



SCHOOL OF ENGINEERING - MICROENGINEERING

SEMESTER RESEARCH PROJECT - Q-LAB

RESPONSIBLE PROFESSOR : PROF. DR. NIELS QUACK
SUPERVISOR : DR. HERNÁN FURCI

Optimization of Bistable Silicon Photonic MEMS
Switch Architectures

Author :
Claudio JARAMILLO

SCIPER:
269808

June 6th, 2021

Contents

1	Introduction	3
1.1	Silicon photonic MEMS	3
1.2	Scope of the project	4
2	Current implementation	5
2.1	Original design	5
2.2	Design criteria	8
2.2.1	Design constraints	8
2.2.2	Optimization criteria	8
3	Design & Development	10
3.1	R&D Methodology	10
3.1.1	Conceptualization	10
3.1.2	Design	10
3.1.3	Simulation	11
3.2	Design 1 : Linear Coupler	11
3.2.1	Concept 1 : Diagonal Coupler	11
3.2.2	Concept 2 : Diagonal Low-Loss Crossing	15
3.2.3	Design 1 : Conclusions and discussion	17
3.3	Design 2 : U-Turn Coupler	18
3.3.1	Redesign of the MEMS coupler	19
3.3.2	Design 2 : Conclusions	20
3.4	Design 3 : Sigmoid Coupler	21
3.4.1	Design 3 : Conclusions	23
4	Performance characteristics and results	25
4.1	Qualitative modeling of the key components	25
4.1.1	Mechanical modeling of the coupler	25
4.1.2	Electromagnetic modeling of the waveguides	27
4.2	Computation of optical losses	34
4.3	Simulations on COMSOL Multiphysics®	35
4.3.1	Buckling mode shape analysis	35
4.3.2	Estimation of the deflection	41
4.3.3	Estimation of the effective stiffness of the couplers	44
4.3.4	Results	44
5	Limitations and discussion	46
5.1	Design limitations	46
5.2	Software limitations	46
6	Conclusions and future prospects	48
References		49
Appendix		50
A	Relaxed uniform cubic B-spline curve description	50
B	Curvature and curvature radius mathematical description	53
C	Mathematical model of the buckling of the MEMS coupler	54

1 Introduction

1.1 Silicon photonic MEMS

Photonics, and photonic integrated systems are devices that use electromagnetic waves (light) as a communication medium. Photonic integrated circuits provide functions such as amplification, routing, modulation, for signals carrying information, and typically operate at optical wavelengths in the near visible spectrum or near infrared 850 nm - 1650 nm.

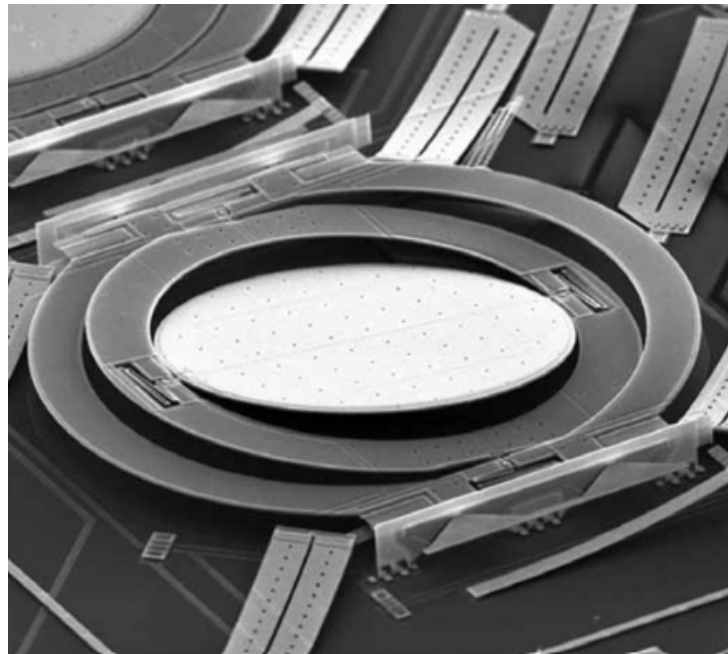


Figure 1: Optical MEMS switch based on a micromirror. [1] [2]

To that extent, optical switches are a crucial element of an optical system. An optical switch is a device that enables switching a given signal between different channels. These switches are usually characterized by the input/output port count, and were often fabricated using mirrors, or reflective coatings. [2] However, it is becoming increasingly feasible to use micro-electromechanical systems (MEMS) as optical switches, to be able to benefit from their high integration capabilities, reliability, robustness, and low power consumption. To ensure that these new technologies are viable economically and fabrication-wise, photonic MEMS-based circuits are built based on the well known and understood silicon fabrication methods used in the electronics industry for the past decades.

By exploiting the mechanical properties of MEMS, we can create a system that exhibits buckling under compressive stress, and therefore creates 2 buckled stable states : we have created

a non-volatile latching switch that requires power only to switch from ON to OFF (or vice-versa).

1.2 Scope of the project

“Silicon Photonic MEMS Switches have recently been shown to be an excellent contender for large-scale photonic integrated circuit switch matrices, for the use in next-generation data centers, telecommunication infrastructure, as well as in space telecommunications [3]. In particular, the possibility to include mechanical bistability, provides access to mechanically stable, unique non-volatile optical configuration states, which has the potential to drastically reduce the power consumption in optical switches [4].”¹

The scope of the project is therefore to investigate different designs for optical MEMS switches, operating in the [1460, 1580] nm range, and to draft the corresponding photonic chip layouts in an actual microfabrication design framework. We will attempt to optimize these MEMS switches’ design based on certain optimization criteria that will be further explained later in this paper, and we will simulate the switches using finite element modeling techniques (FEM) to explore their buckling mode shapes.

In this paper we present 3 optimized optical MEMS switch architectures, their design philosophies and decisions, as well as their possible implementations in switch array grids for applications in data centers, telecommunication infrastructure or aerospace telecommunications.

¹As stated by Prof. Niels Quack.

2 Current implementation

2.1 Original design

The project expands and optimizes previous work that had been done by Prof. Dr. Niels Quack, and Dr. Hernán Furci, where a first design for a MEMS switch was proposed. The general design philosophy is to create a unit cell with 2 input and 2 output ports, that can be duplicated and thus form an array of unit cells creating an $N \times N$ switch array.

The switch unit cell is composed of 2 main elements : the MEMS coupler, and the waveguide that carries the signal on the substrate. On this paper it will be referred to as “bottom waveguide” (BWG). The coupler moves vertically in the z-direction, where the ON state is when the coupler is down, and the OFF state is when the coupler is up. The original design shows a unit cell with straight bottom waveguides which is ideal to minimize optical losses. To couple the light from one channel to the other, the MEMS coupler is designed with a 90° bend. Each unit cell can be individually addressed by using row/column addressing on each of the cell’s electrostatic actuators.

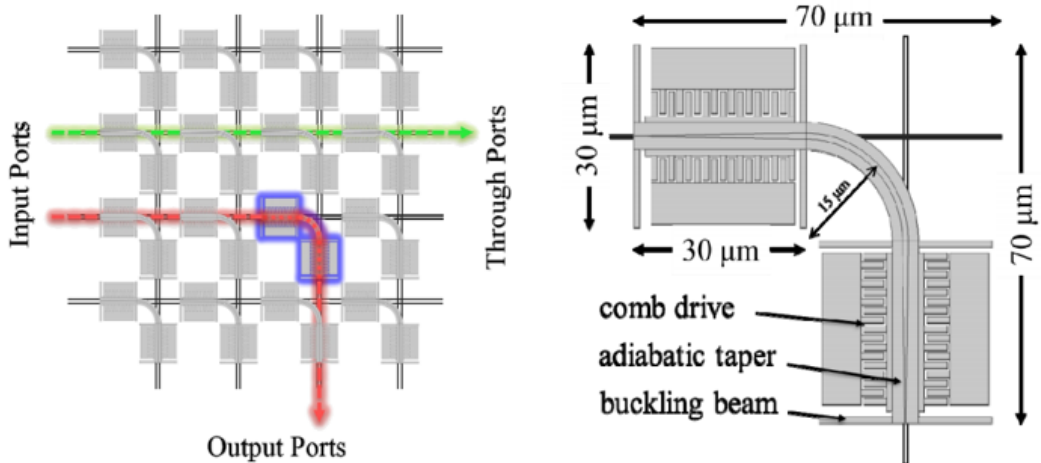


Figure 2: Schematic of the original 90° bend design. Left : possible paths taken by the light, and schematic view of the array. Right : schematic view of a 90° bend MEMS coupler. [4]

The original design’s coupler is made up of 2 comb drive actuators that are actuated out-of-plane together. They actuate the coupler’s waveguide, which is suspended by 4 buckling beams per actuator, and who are both joint together by the aforementioned 90° waveguide bend. The coupling between the bottom waveguide and the coupler’s waveguide is carried out by evanescence of the electromagnetic field in the vertical z-direction. The coupling is directional and adiabatic, which is obtained by tapering the coupler’s waveguide across a length of 30 μm in opposing directions depending on whether the light is being coupled in or out of the coupler.

For example, the tapering required to adiabatically couple light out of the coupler is from wide to narrow.

Buckling of the structure is obtained because of residual stress on the substrate during the fabrication procedure. The buckling beams are therefore used as the sources of compressive stress, and as the element guiding and constraining the coupler's movement when transitioning from ON to OFF.

The buckling beams therefore apply compressive stress on the structure in 2 different directions (x and y). It has been shown that applying bi-axial stress is a problem of the original design, and can lead to torsion, or instabilities during the displacement of the structure. The original unit cell has dimensions of $110 \times 110 \mu m$, which could potentially be optimized and reduced. By reducing the footprint of the structure it is also possible to reduce the size of the coupler, therefore increasing its stiffness, and achieving a faster switching speed. The switching time of the original design is $0.91 \mu s$.

The optical losses of the current design are quite low, since the geometry of the bottom waveguide is made up of only straight lines. When a waveguide bends, the wave it carries experiences radiative losses, and the tighter the bend (the smaller the radius of curvature) the more losses. The bottom waveguide is also characterized by the presence of a low-loss multimode interference crossing. It is a routing element that allows two waveguides to cross each other while maintaining minimal crosstalk between themselves. The biggest contributors to optical losses are therefore the crossing, any bends on the waveguides, and the coupler itself. This will be further explored in section [4.1.2](#)

The first estimations put the propagation losses of the waveguides to 1.1 dB/cm , however, further research by Dr. Hernán Furci showed that the losses measured experimentally were of around $1.5\text{-}1.6 \text{ dB/cm}$. The optical loss for the low-loss crossing is estimated to be $0.017 \text{ dB/crossing}$, and the total loss for a unit cell is estimated to be 0.025 dB/cell . The switching loss (from the coupler) is estimated to be 0.47 dB .

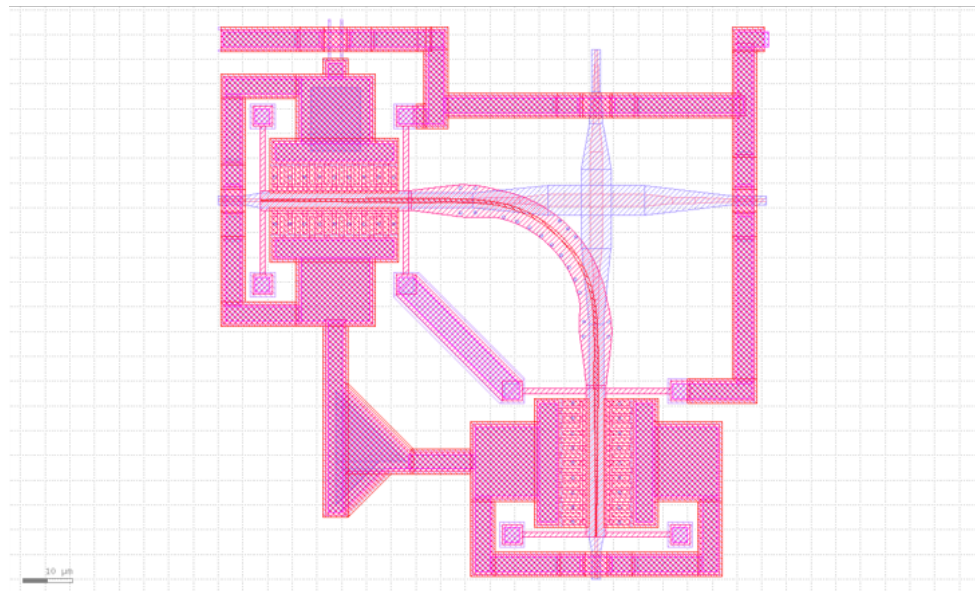


Figure 3: 2D image of the original design's unit cell on K-Layout. [4]

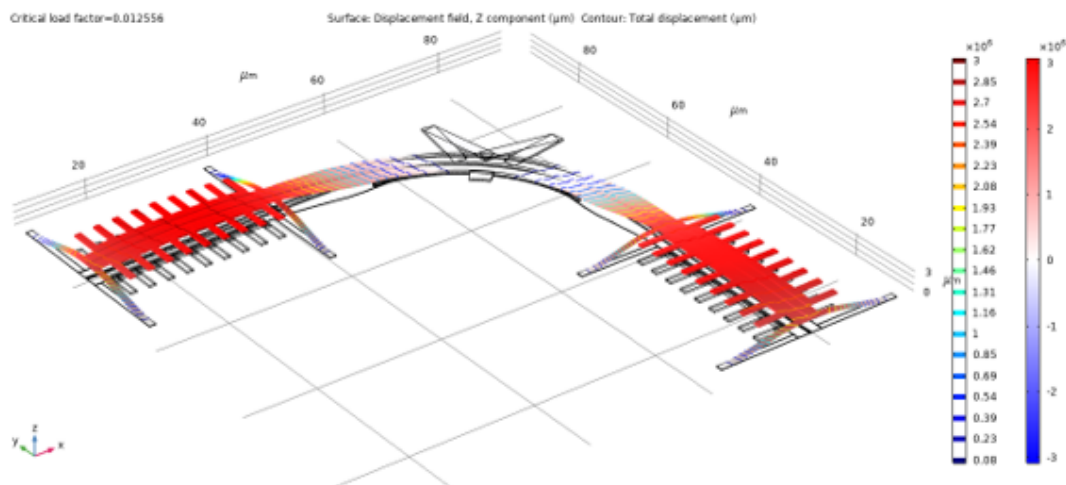


Figure 4: COMSOL simulation results of the first buckling mode shape for the original coupler. [4]

After all the previously mentioned considerations we can build a set of design constraints and optimization criteria upon which new designs will be based.

2.2 Design criteria

2.2.1 Design constraints

The constraints of the design are as follows :

- The low-loss multimode crossing will not be modified. The current design has proven to be effective and reliable, and no modification will be done to it. [5]
- The comb drive actuators and buckling beams will not be modified unless absolutely required. They have been carefully designed and optimized, and their operation has been demonstrated to be effective. Unless a design could benefit, or requires a redesign of the comb drive actuators, they will not be changed.
- Each cell must be individually addressable. To achieve this we will implement a similar structure to the one that has already been implemented using row/column addressing in the chip.
- Any path taken by light will *at most* go through 1 coupler. Indeed, one of the main objectives of this project is to provide a switching solution with minimal losses. Since the coupler introduces by far the biggest optical loss, and to keep the current design's architecture as a $N \times N$ array, we will only consider designs for which there is at most 1 coupler in the optical path.
- Rib waveguides are preferred and are widely used in the original design. When possible it would be preferable to use rib waveguides as these exhibit lower propagation losses than strip waveguides. Strip fully etched waveguides however enable the use of lower radii turns, thus creating more compact photonic circuits. We will use fully etched strip waveguides for any tight turn (radius smaller than 15 μm).

2.2.2 Optimization criteria

After considering the original decisions, and the design constraints that dictate the limitations and directions of any future unit cell and coupler designs, we can set-up a set of main optimization criteria with which we can quantify the quality of any new design, and to which we can refer back when developing a new design and comparing it to others.

- **Uniaxial stress only** : it is crucial that any new design exhibits uniaxial stress only, to avoid unwanted mechanical instabilities, torsion, etc. By aligning the buckling beams along the same direction we can achieve this goal in general.
- **Smaller footprint** : the current unit cell size is around $70 \times 70 \mu\text{m}$, this can be reduced, and we will attempt to minimize the size of all elements in order to reduce the overall footprint of a unit cell.

The main strategy that will be used to achieve this design constraint will be to modify the geometry of all possible elements, such as reducing the radius of bent waveguides to create a tighter fit between all elements, or re-arranging the elements of the unit cell in order to achieve a more efficient use of space.

- **Increase switching speed** : the switching speed is a parameter that can be related to the size of the coupler. The smaller the coupler, the stiffer and therefore the quicker the transition between the ON and OFF states can happen. Therefore by reducing the footprint size we should be able to increase the switching speed subsequently.
- **Low optical losses** : it has been estimated that the optical losses for the current design are of around 0.026 dB/cell, with a switching loss of 0.47 dB. It is required that any subsequent design exhibits similar optical losses. More details will be given in section 4.1.2

The main strategy to maintain low optical losses will be to use curvature matching strategies when transitioning from a straight waveguide to a bent waveguide [6] [7], while minimizing the distance the light has to travel to a cell to reduce the propagation losses. The use of strip-rib waveguide transitions is a tool that will also be used to enable the creation of tight turns while also minimizing optical losses.

The switching loss will inherently be similar to the original design, as the adiabatic tapered coupler will largely remain untouched, and the coupling distance will be similar or smaller.

As in any engineering design project, these optimization criteria are guidelines that must be weighted against each other in order to find a compromise.

3 Design & Development

3.1 R&D Methodology

The work required for the design and optimization of our silicon MEMS switches can be divided in 3 parts : conceptualization, design, and simulation.

3.1.1 Conceptualization

The design of a new concept starts on paper, designing geometries and architectures. The conceptualization phase is extremely important because it sets on paper a switch design on which hours of work will be put into. Each design is then openly discussed with the project supervisor, and responsible professor before continuing onto the design process. Collaboration and sharing ideas is an integral part of this process. Once a design has been green lit, and therefore is worth being developed, we move onto the design phase.

3.1.2 Design

The design phase is performed by implementing the ideas and concepts put forward into a qualitative model. MATLAB [8] and L-Edit [9] are used to implement those ideas. Prior work done by Dr. Furci helped streamline the process as some geometrical elements characteristic of the unit cell's design (such as waveguide generation using a GDSII library for MATLAB) were already setup. Therefore, the design of specific elements such as curvature matching splines, or certain turns are generated using MATLAB.

Any other simple element, such as circle arcs, or rectangles are generated on Mentor Graphics' L-Edit software for IC design [9]. It is perhaps important to note that L-Edit is a software that exhibits a lot of instabilities, has trouble exporting and importing files that have not been created on the software itself (for example, if a GDSII file is created by MATLAB, it will be affected), and wrongly displays certain objects' geometries. To that extent, verifying the validity of the MATLAB generated objects will first be done on K-Layout [10], since the software seems to be much more stable and has better compatibility with these sorts of elements.² After a model has been designed and fulfills all the desired requirements, it can be exported and simulated.

²It would seem like the problem arises from the fact that L-Edit does not deal well with geometries that are different from circles and rectangles, or any combination of the two. Certain cubic splines show artifacts at the edges and corners, as well as sinusoidal segments. These elements were created in the interests of curve matching.

3.1.3 Simulation

An exported design is loaded onto COMSOL Multiphysics © [11] where it is 3D-modeled, and it is simulated. 2 simulations are performed : the first is a linear buckling simulation, where we can extract the geometry of the buckling modes of the structure that has been exported and therefore verify it's usefulness as a bistable switch. To then understand if the switching amplitude is as required, we also perform a stationary study of deflection, which will yield the buckling distance of the beam. The simulation aspect of the project will be explored more in detail in the following section.

3.2 Design 1 : Linear Coupler

3.2.1 Concept 1 : Diagonal Coupler

Originally proposed by Dr. Furci, this design solves the issue of removing bi-axial stress by modifying the bottom waveguide (BWG) in such a way so that a linear coupler can be placed at an angle and couple the light in between channels.

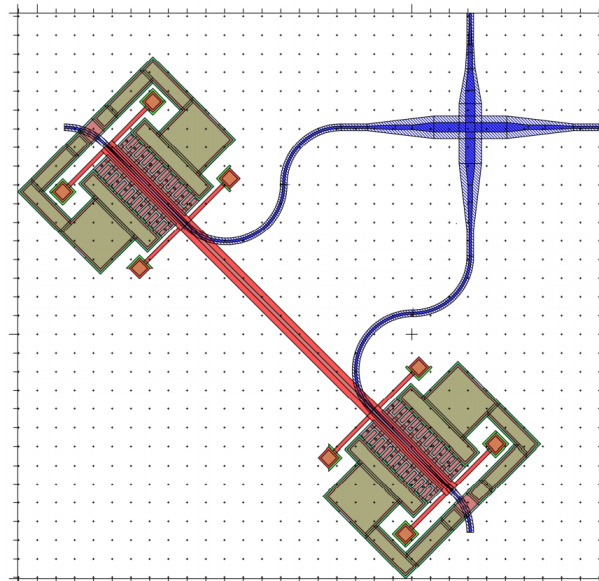


Figure 5: First rough implementation of the Linear Coupler design. Tick scale : 5 um. Row/column addressing not implemented.

A first implementation using simple circle arcs shows that indeed this design is compatible

with the requirements stated previously, however some aspects must be further optimized.

First of all, there is a large amount of unused space in between the coupler (red in fig. 5) and the low-loss crossing (blue in fig. 5). Second of all, the coupler length is quite high. This may lead to some problems : the longer the coupler, the more probable it is that multiple mechanical buckling modes, or torsion modes exist near each other and therefore the system might be unstable under actuation. A longer coupler is also decreasingly stiff, and therefore the actuation speed is going to be lower compared to a shorter equivalent. Finally, a longer coupler is clearly more massive, and therefore requires more electrostatic force to actuate.

3.2.1.1 BWG modification using 3rd order Bézier curves

The first solution proposed to address the issue of unused space and improve miniaturization of the cell, is to design the bottom waveguide (BWG) as a 3rd order Bézier curve with a set of constraints. Bézier curves are parametric curves, which are related to Bernstein polynomials, and are named after Pierre Bézier, who used them in the 1960s for designing curves for the bodywork of Renault cars. [12]

This mathematical object has the distinct advantage of being able to fulfill all the requirements concerning curvature matching : they have 0 curvature at the end points of the curve, are continuous, have continuous curvature, and are procedurally generated. The object we generate is called a relaxed uniform cubic B-spline curve. The main advantage is therefore that a single mathematical object fulfills all the conditions, and also can be generated to fit many other geometries quite easily.

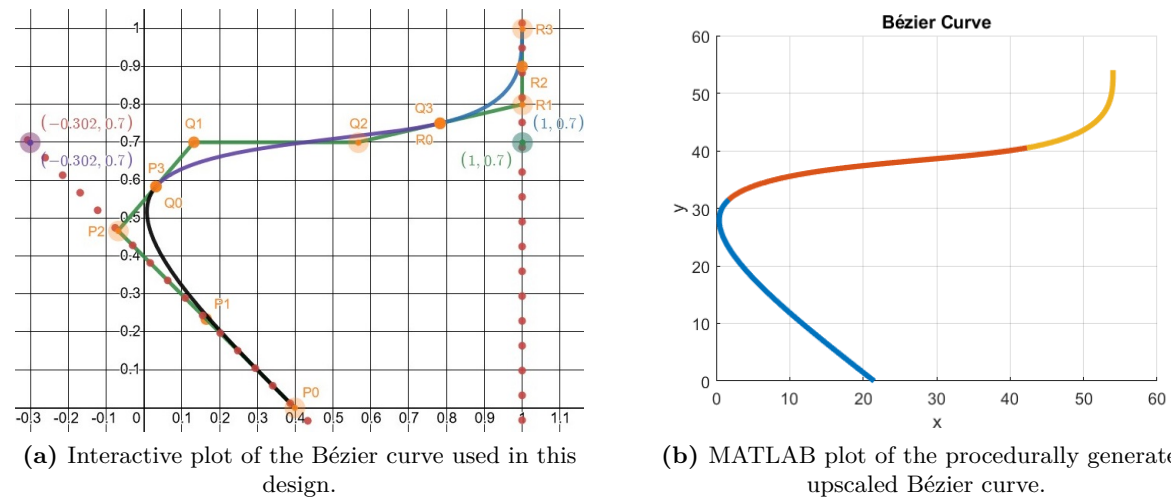


Figure 6: Plots of the relaxed uniform cubic B-spline curve used in this design.

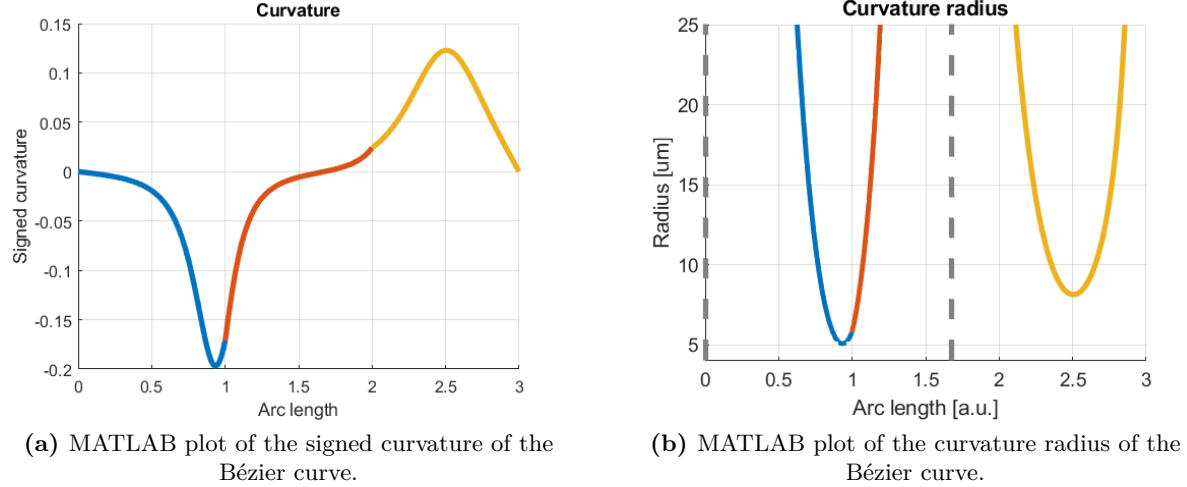


Figure 7: MATLAB plots of the curvature characteristics of the generated Bézier curve.

This particular curve is contained within the [1;1] square and is therefore easily scalable. It consists of 3 joint B-splines, with curvature matching at each joint. This particular design has been optimized to only have 5 DOFs : the x-coordinates of points P0, P2, and Q2, and the y-coordinates of points Q2 and R2, according to the plot in fig. 6. The way these coordinates must be chosen is further explained in appendix A. The resulting BWG is shown in fig. 8

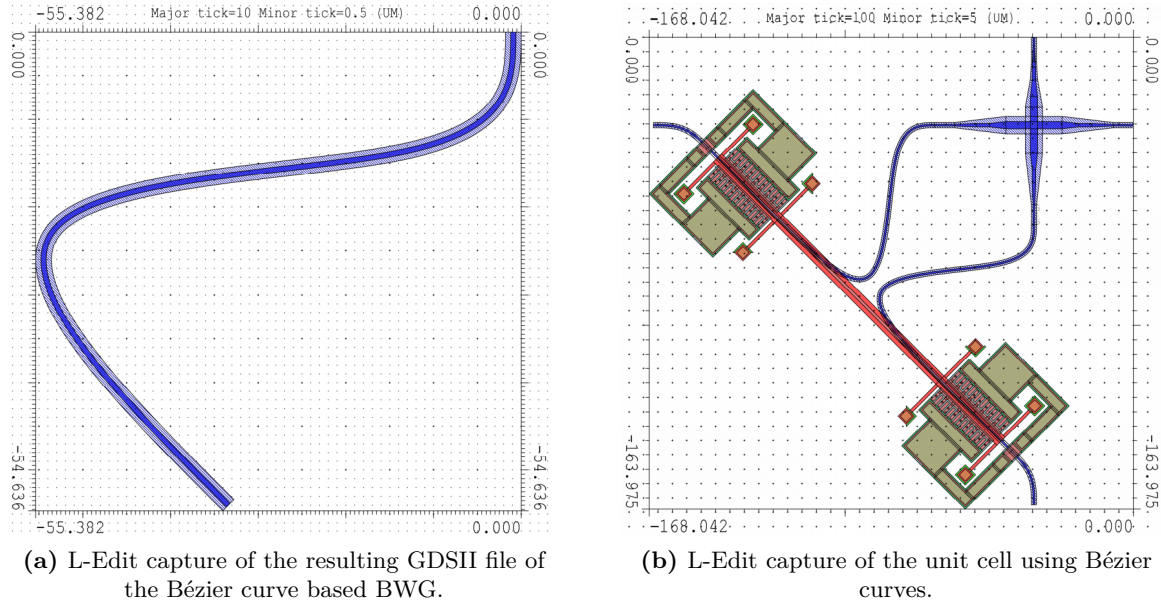


Figure 8: Unit cell elements using BWGs based on relaxed uniform cubic B-spline curves. Rib waveguides used.

Despite providing an elegant solution, and reducing the amount of unused space compared to a first implementation, these splines also require that the coupler used must be quite long. In fact the coupler is 79 [μm] long, which is excessive. As expressed previously, a long coupler must be avoided.

3.2.1.2 BWG modification using circle arcs and sinusoidal curvature matching

The second solution proposed is to modify the BWG by using a certain number of pre-designed waveguide segments. These segments are functional modules that can be generated using MATLAB individually. They are then imported into L-Edit and stitched together manually. Despite this solution requiring additional work from the designer's part to build the required geometry, and requiring multiple individual segments to produce a finished waveguide, it has the advantage of being highly modular, and therefore also being easily adaptable.

In this case we use a set of sine-circle-sine matched bends of 90°, 315°, 135° of rotation. Similarly to the Bézier curve, this design does not show a single continuous change of curvature across the entire length of the BWG, but rather across each of the segments that compose it, with matched curvature at each boundary. The resulting geometry can be found in fig. 9

As for the previously shown design, this geometry still exhibits quite a large amount of unused space. Even when considering that the row/column addressing for the comb drives are not shown, the blank space between the coupler and the low-loss crossing will undoubtedly remain unused.

By trying to push the coupler closer to the low loss crossing we encounter the main limiting factor in this design : the geometry requires that there exist 2 lobes on the BWG that by design are diagonally mirroring each other, therefore as one tries to push the coupler it becomes inevitable that the two lobes overlap each other.³ It is also evident that as we push the coupler closer to the low-loss crossing, the required radius of the bends on the BWG become increasingly small. At the limit of a radius of 5 [μm] for all relevant bends, and pushing the lobes as close to each other as possible without overlap, we can clearly see that this design philosophy will not be viable as a more compact solution. This is seen in fig. 10.

After exploring this design philosophy, it seems clear that a new paradigm on the integration of the low-loss crossing is required. We will therefore explore an alternative design in which we modify the low-loss crossing's orientation within the unit cell in order to optimize the footprint of the unit cell.

³Using a second low-loss crossing to address this problem was briefly considered, but as such a crossing introduces additional unwanted optical losses, it was quickly dismissed.

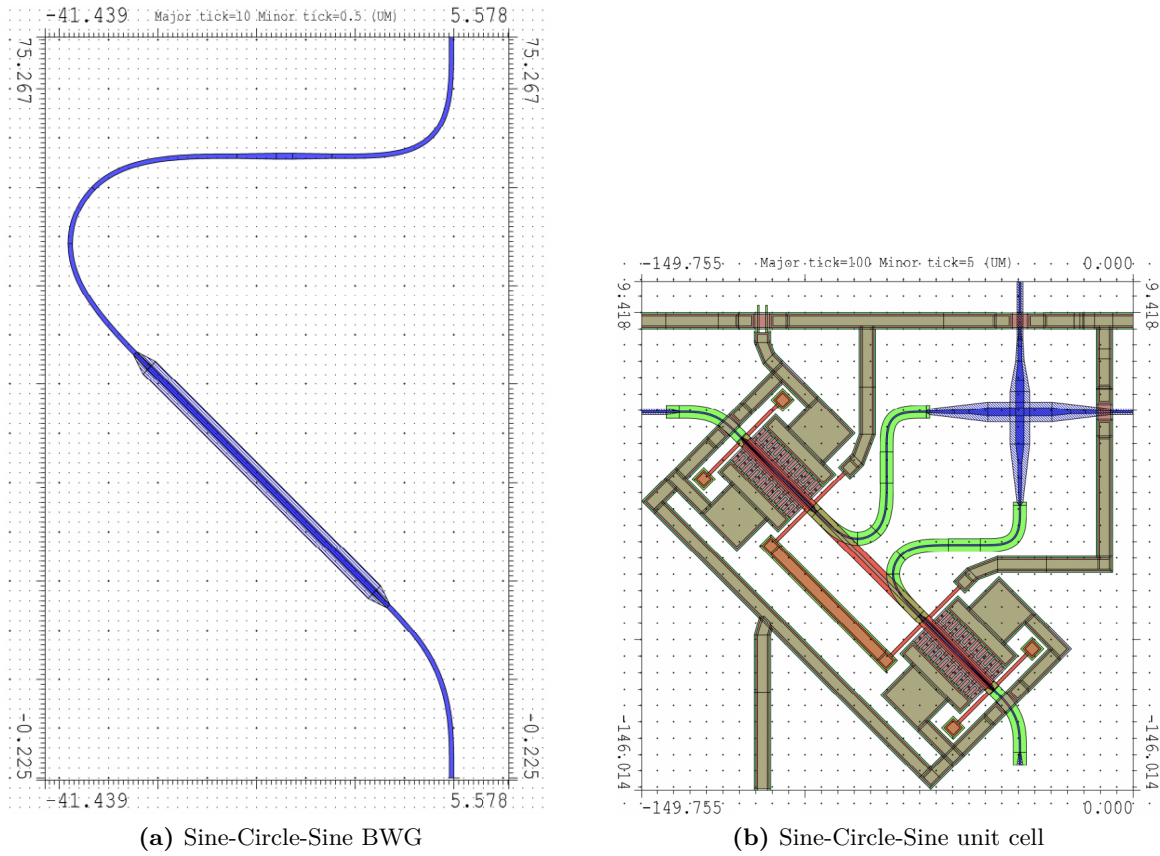


Figure 9: Unit cell elements using Sine-Circle-Sine curve matching strategies for the BWG. Rib and strip waveguides used. No row/column addressing shown.

3.2.2 Concept 2 : Diagonal Low-Loss Crossing

We propose a modification to the design paradigm of the linear coupler, by rotating the low-loss crossing by 45 degrees. We therefore will have a horizontally aligned coupler, and we will use the predefined modules in paragraph 3.2.1.2. The resulting design is shown in fig. 11.

To achieve the unit cell's geometry integration necessities (i.e. being able to build a matrix), the BWGs are modified using the same 90° , 135° and 315° bends as before, and are bent to match the in/out port's relative height.

The linear coupler is once again linear, and has a suspended length of 66.8 [μm] long. We have sacrificed some miniaturization potential in the coupler in favor of attempting to create a more compact BWG design.

This design achieves the goal of pushing the MEMS coupler as close as possible to the low-loss crossing, and therefore we achieve the limiting length and footprint to that extent.

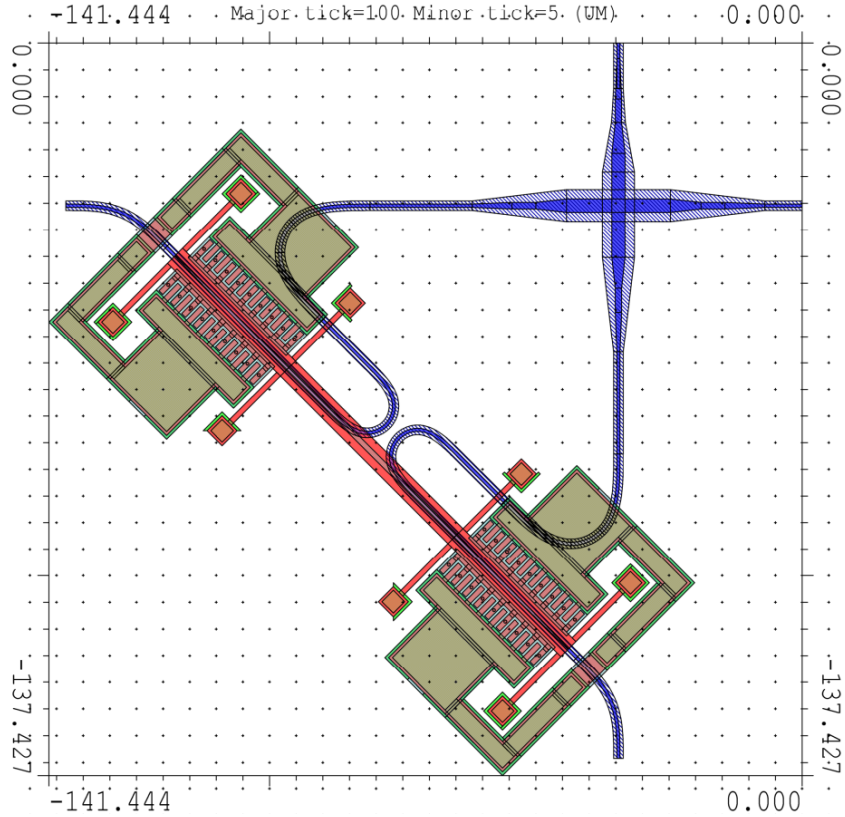


Figure 10: L-Edit capture of the limiting dimensions when trying to approach the coupler to the low-loss crossing.

However this induces the necessity of adding some tight turns to all of the BWG elements, and more specifically, any optical signal that passes through a cell without being coupled. These added optical losses are highly problematic, as they do match in order of magnitude the losses induced by the low-loss crossing. This therefore allows us to immediately discard this design, as having twice the optical losses per cell is unfeasible.

It is also quite interesting to note that with this design philosophy we reach a point where the MEMS device has the same size as the low-loss crossing.

In order to improve the optical performance of this design, we explore a solution in which the input/output ports of the vertical and horizontal lines are not aligned, and therefore the resulting matrix would have to be staggered. However, it is in general a bad design idea to do as such, since when building an array of such cells the resulting geometry will be very elongated, and therefore will exceed the chip's dimensions.

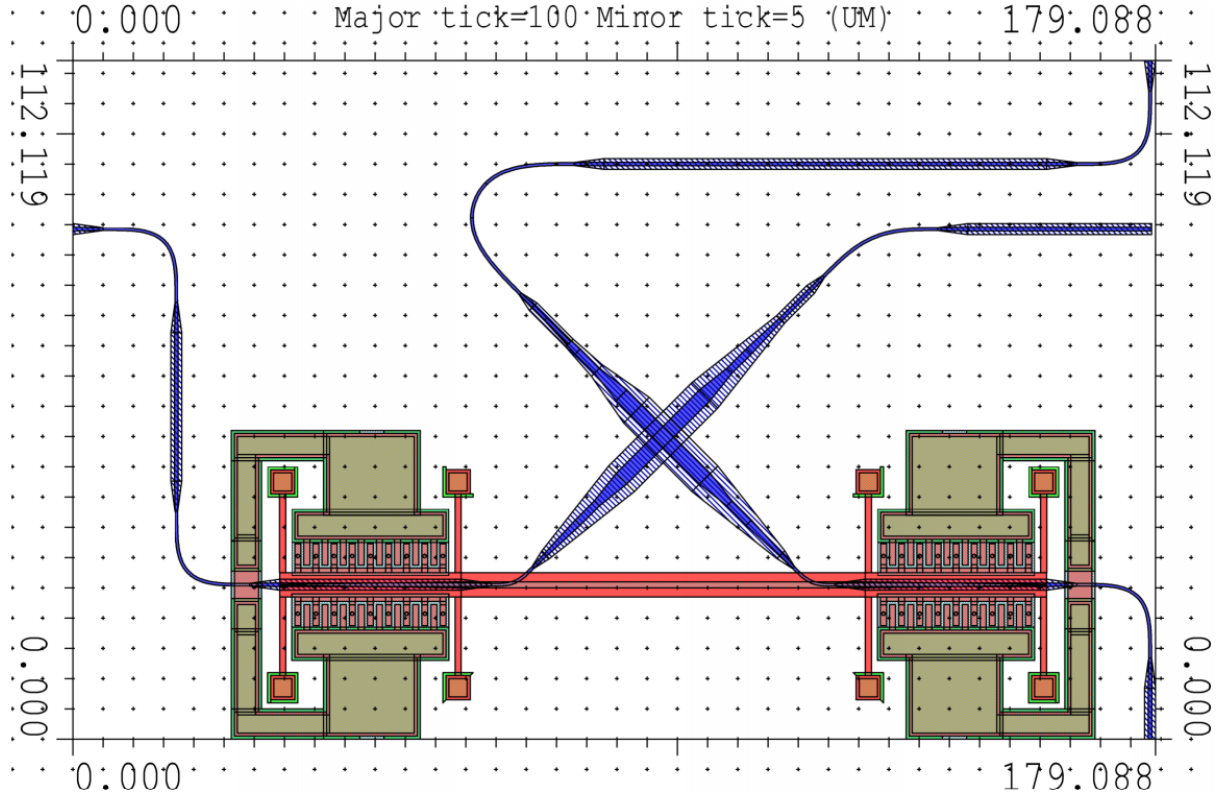


Figure 11: L-Edit capture of the unit cell incorporating a diagonal low-loss crossing.

3.2.3 Design 1 : Conclusions and discussion

For all Linear Coupler designs based on the diagonal coupler philosophy, a shared problem is the BWG losses. The concept intrinsically requires that both the “Through” WG and the “Output” WG (cf. to fig. 2) both are mirrors of each other, and exhibit 3 turns, with a radius of 5 [μm], and high turning angles, these modified BWGs therefore must be fully etched, at a width of 450 [nm]. This means that regardless of the path the light follows, it will pass through a section of WG with high optical losses.

Both designs also exhibit excessive BWG path lengths. Since the highest length optical path will go through $2 \times 63 = 126$ cells, such structures with tight bends, and rib-strip transitions will always induce higher optical losses than the original design, despite trying to curvature-match, and despite using tapers for rib-strip transitions.

Regarding the use of Bézier curves for the creation of waveguides, it might be useful to use this design philosophy for other applications, where miniaturization requires “exotic” routing of waveguides within a photonic integrated circuit (PIC). They are also easily modifiable, as a Bézier curve constructed by joint segments of other B-spline curves has the property of being highly adaptable segment per segment. However it is certain that these objects have

the limitation of only being useful for very specific designs, where modeling the path of light using such curves is possible, and they must be manually tweaked on a “per application” basis. Furthermore, as opposed to the use of waveguide segments, it is not feasible to create a library of modules that could be accessible and used independently of each other, for example. By their very nature, Bézier curves also have the disadvantage of often exaggerating the *rate of change of curvature* when dealing with tight turns, and therefore might induce increased losses as opposed to using pre-designed modules.

3.3 Design 2 : U-Turn Coupler

Originally conceptualized by Prof. Niels Quack, we propose a design where we have an optical coupler in a U-Turn shape. The main objective of this design is to minimize the footprint of the MEMS device, and attempt to push the BWG as close to each other as possible. In this design we keep the BWG’s low-loss crossing in its original orientation and we modify the BWG to accommodate the new coupler’s geometry.

The coupler has been modified with a 5 [μm] U-Turn sine-circle-sine matched curve. It is important to note that this curve does not show a reduction in the waveguide width, as recommended by the researchers who first proposed this technique. [6] [5] The reason we made this design decision, is because we want to maintain the confinement of the light in the coupler once it has been coupled up. Since the suspended part of the coupler passes over the BWG and the low-loss crossing, it is important to insure that there will be no light being coupled back down into the BWG. Keeping a large waveguide width with respect to the lower BWG helps maintaining the light’s confinement.

The coupler’s 5 [μm] U-Turn is fully etched, and therefore includes a taper to transition from the rib waveguide to the strip waveguide. It is worth mentioning that to attempt to reduce the overall coupler’s size, and to avoid any possible out coupling of the light from the coupler’s suspended section into the BWG, we have achieved a more compact taper, to the expense of optical losses.

All of our BWG elements follow the same philosophy of designing a set of modules that are then used multiple times in the design. Therefore we have built modules for 45° turns, 180° turns, tapers, etc. The resulting unit cell is shown in fig. 13.

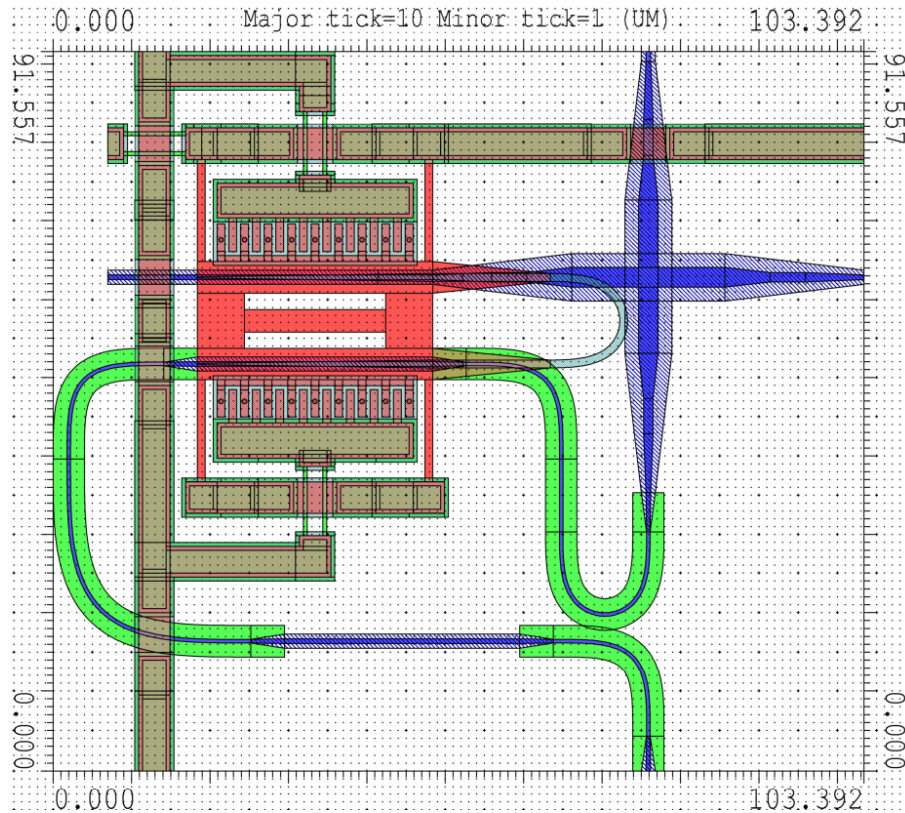


Figure 12: L-Edit capture of the U-Turn coupler design. Fabrication layout shown.

3.3.1 Redesign of the MEMS coupler

The U-Turn design requires a redesign of the MEMS coupler. In order to achieve the smallest acceptable radius of $5 \text{ } [\mu\text{m}]$ for the suspended U-Turn on the coupler, we were required to modify the geometry of the comb drive actuators, as well as a redesign of the coupler itself.

We decided to remove the “inside” comb actuators, so that the inlet and outlet taper regions on the coupler are actuated by two comb drives only. In order to maintain the stability and rigidness of the MEMS coupler, we join both tapering regions together with two silicon cross bars that act mechanically as anti-roll bars. They help maintaining the in and out tapers at the same roll rate at both ends of the tapering regions. In order to maintain constant roll across the whole surface, and increase the stiffness of the coupler, we also include a joining bar in between both anti-roll bars to strongly couple them together and therefore reduce the possibility of torsion across the device.

The design of the suspension arms, and the comb drives remains the same. The distance between the comb drives has been reduced to the minimum possible distance of $5 \text{ } [\mu\text{m}]$ for the

coupler's U-turn, and the BWG has been modified to accommodate this.

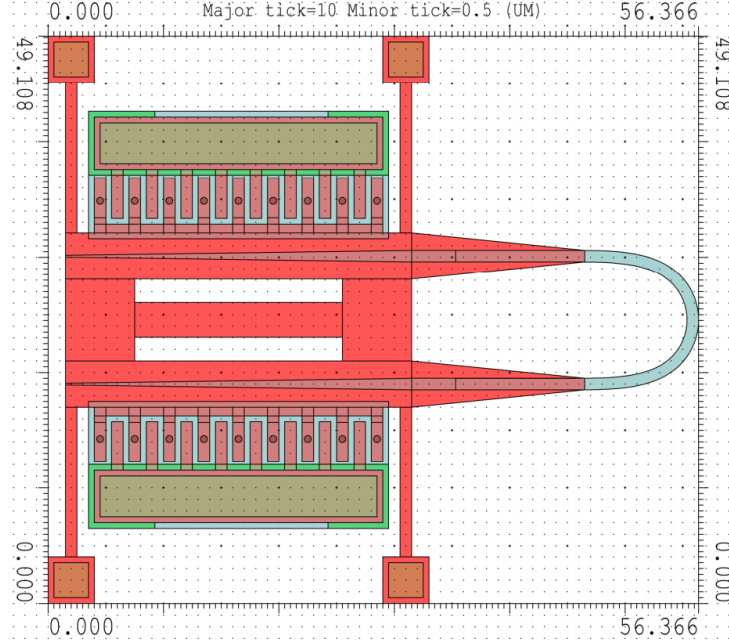


Figure 13: L-Edit capture of the U-Turn coupler, with redesigned MEMS.

3.3.2 Design 2 : Conclusions

The design of the U-Turn coupler seemed promising since the beginning of the design process. The redesign of the MEMS coupler is the biggest challenge and the main source of work for this design, since the modules needed for the redesign of the BWG had been previously created during the development of Design 1 in section 3.2.

It is quite interesting to note that once again we reach a point where the limiting element of the unit cell is the low-loss crossing. In fact the MEMS device could be miniaturized further, however making a coupler that is much smaller than the low-loss crossing makes little sense since this would require a complete redesign of the crossing and would need to introduce tight curves in the BWG as we have seen in the previous figures.

Design has the distinct advantage of using the smallest MEMS coupler designed in the project, and as long as we aim to keep the same optical losses it seems unreasonable to attempt to miniaturize it even further. Therefore, if this design could be applied to another project where the biggest element is the MEMS and not an optical device such as the low-loss crossing, it could provide a compact solution for light coupling between channels.

3.4 Design 3 : Sigmoid Coupler

Originally proposed by C. Jaramillo, and approved for development by Prof. Niels Quack, this design aims to use a *logistic sigmoid function* as a basis for the geometry of the optical coupler.

A logistic sigmoid function has the distinct advantage of being an S-shaped function with an easily controllable set of parameters such as : the curve's length, the slope, the curve's height, and the central point. The function is given by :

$$y = \frac{a}{1 + e^{b \cdot (x - x_0)}} \quad (1)$$

Where the function's length is defined by the bounds for x , b is the slope factor, a is the height, and x_0 is the central point.

In this case we chose to have a length of 46 [μm]. This is chosen by the fact that the limiting length of the coupler, given by the BWG's low-loss crossing is 39.607 [μm]. We simply approximate that length to 40 [μm] and add 3 [μm] on either side of the coupler as a buffer length between the different optical elements.

The slope is chosen by sweeping over all values of the slope b until we obtain a minimum curvature radius of 5 [μm] to fulfill the optical losses and compactness requirements. We obtain that $b = 0.555$.

The height is limited by the low-loss crossing, as we cannot possibly make a shorter coupler. We therefore chose the limiting length of $a = 39.607$ [μm].

We chose the central point to be $x_0 = 0$, and the coupler is defined for symmetric positive and negative values of x , from $[-23, 23]$ [μm].

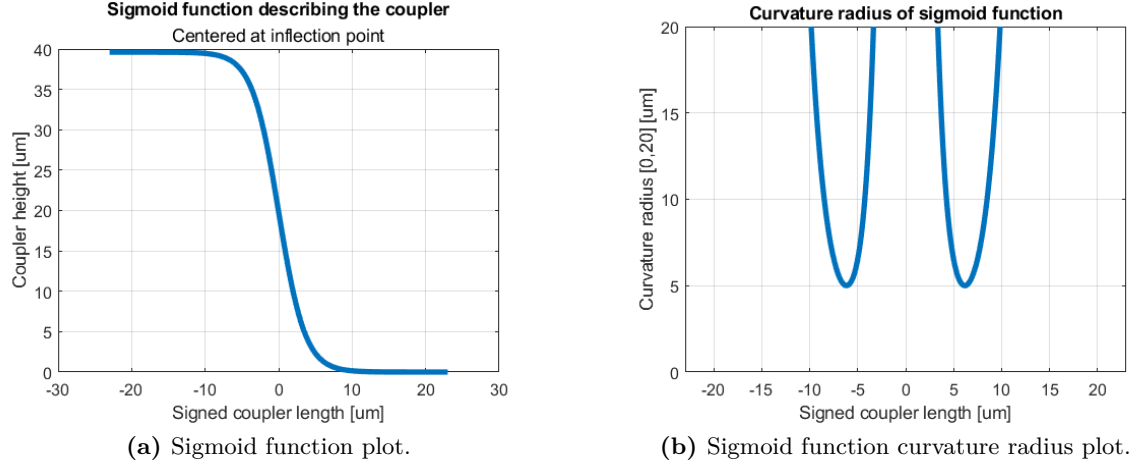


Figure 14: MATLAB plot of the sigmoid function describing the coupler. Defined for $-23 < x < 23$, and minimum curvature radius of 5 [μm].

The details on the computation of curvature will be explored in appendix B.

The resulting coupler's geometry is shown in fig. 15, and the resulting unit cell is shown in fig. 16. In these graphs we can see how it is required to create a taper from rib waveguide to strip waveguide on the suspended part of the coupler. Indeed this is required since we know from fig. 14 that the curvature radius dips to 5 [μm]. Even though the curvature in the sloped part of the coupler tends to 0, and we could potentially create another adiabatic transition taper between waveguide types, it is not advisable since it will increase the suspended mass of the coupler that needs to be displaced, and therefore negatively impact the mechanical dynamics of the system. Total displacement will be reduced, the force required for actuation will be increased, and since it will be a higher mass suspended by small rods, it can create additional resonance modes that are unwanted.

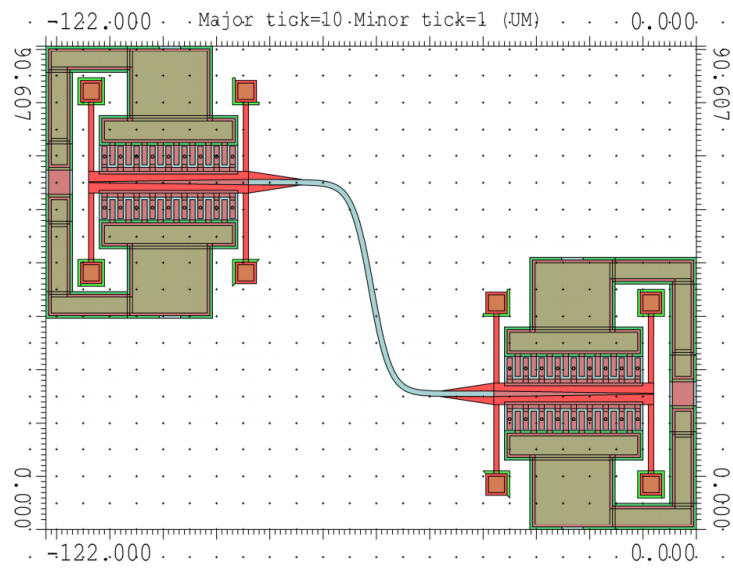


Figure 15: L-Edit capture of the Sigmoid coupler design. Basic layout shown.

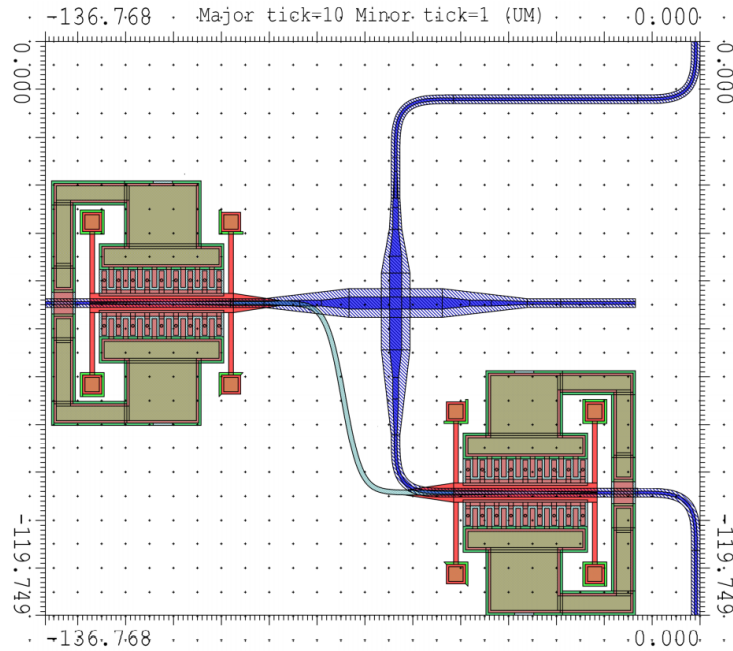


Figure 16: L-Edit capture of the Sigmoid coupler unit cell. Basic layout shown.

3.4.1 Design 3 : Conclusions

Design 3 is a design that, once again, reaches a point where an optimization of the basic geometry that describes it (ie. the sigmoid coupler) turns the bottom waveguide's low loss crossing into

the limiting element for the unit cell's total footprint. Indeed the way we built the coupler is by setting the height of the coupler to the exact same height of the low loss crossing itself, and therefore keeping the same design philosophy we cannot miniaturize it any further. We encounter the same limiting factor as for both of the other designs.

Furthermore, without necessarily performing mechanical simulations on the sigmoid coupler, since the optical coupler is fully etched and quite thin, and because of the sigmoid geometry introducing 2 very tight turns on the suspended part without proper suspension, we can predict that the coupler will be mechanically unstable under buckling. We will confirm this hypothesis in section 4.3.

This design is nonetheless quite elegant, as once again the coupler is described by a mathematical function that perfectly respects all the conditions concerning curvature, continuity, etc. that we require from such a coupler. It is also easily adaptable to many other types of geometries, since the size is controllable by the function's parameters. If the low-loss crossing is modified, or if we apply this design to a PIC where the coupling length is overall smaller, then the mechanical stability of the coupler could be improved, and therefore such a design can be implemented. This design could also be used for a larger coupler, where we do not need to fully etch the coupler's waveguide and therefore we could use a stiffer suspended part that would be mechanically stable. Adding suspension elements could be another way of implementing this design philosophy into another application, but the complexity in fabricating such suspensions could be a challenge.

To conclude on **Design 3**, it seems like the current implementation sits in a size range where a sigmoid coupler is both too big, and too small to be effective, reliable, and predictable. Despite being able to reach the limiting parameters of the unit cell's size, i.e. the low-loss crossing, the mechanical aspect of this design is not sturdy and reliable enough to be implementable.

4 Performance characteristics and results

4.1 Qualitative modeling of the key components

4.1.1 Mechanical modeling of the coupler

In this section we show a model for the mechanical characteristics of the coupler. The coupler is composed by a long main beam, where the waveguide lies, and aligned in the direction of the beam, and 4 suspension beams for each comb drive used to actuate the MEMS device.

The suspensions, or buckling beams, are the elements that actually define the total displacement of the MEMS, not the main beam. The residual compressive stress on the substrate, required for buckling is applied on the buckling beams in their longitudinal direction.

Despite the total length of the MEMS in the direction of the beam being : $2 \times L_{Beam} + w_{Coupler} = 2 \times 13 + 4 = 30 \text{ } [\mu\text{m}]$, we actually only consider a total beam length of $2 \times L_{Beam} = 26 \text{ } [\mu\text{m}]$, since we consider that the main beam (coupler) is far more rigid than the buckling beams and does not bend.

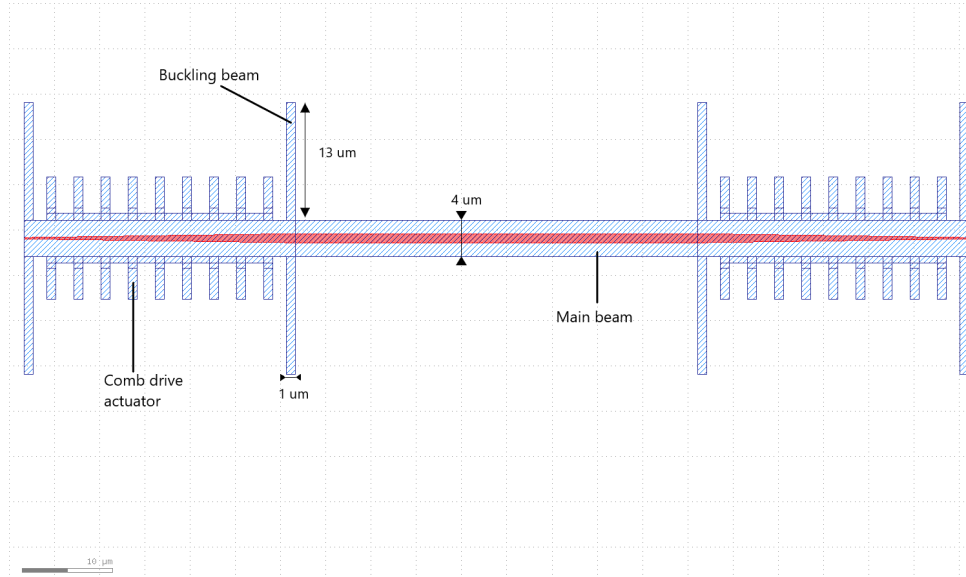


Figure 17: Geometry of the mechanical model of the linear coupler. Red : waveguide. Blue : Mechanically stressed substrate.

For the U-Turn coupler, we have a length of : $2 \times L_{Beam} + w_{Coupler} = 2 \times 13 + 15 = 41 \text{ } [\mu\text{m}]$.

We also consider the fact that we needed to modify the geometry of the comb drive actuators, and therefore we have a total of 4 suspension beams for the entire MEMS coupler, whereas for the linear and sigmoid coupler, 8 suspension beams are used in total.

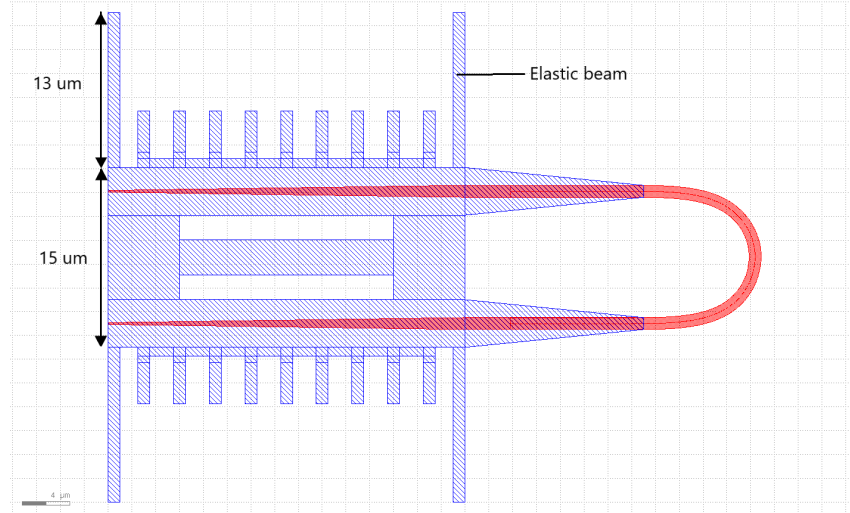


Figure 18: Geometry of the mechanical model of the U-Turn coupler. Red : waveguide. Blue : Mechanically stressed substrate.

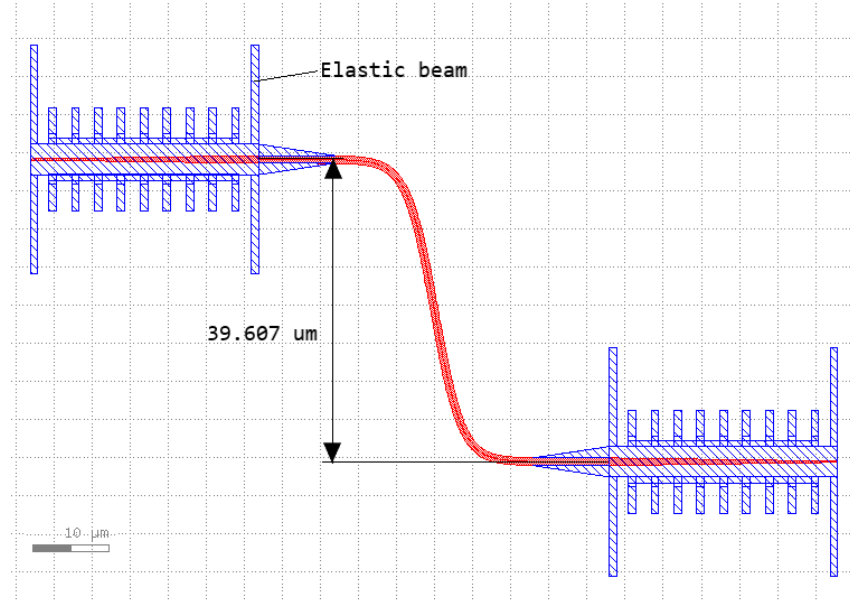


Figure 19: Geometry of the mechanical model of the sigmoid coupler. Red : waveguide. Blue : Mechanically stressed substrate.

We can thus use the theory put forward in appendix C to perform a qualitative analysis of what the mode shape of the beams will be.

Referring back to fig. 17, and based on appendix C, we can compute the rigid proportional length of our MEMS devices :

1. Linear Coupler :

$$Prop_R = \frac{l_{tot}}{l_R} \approx 0.13 \quad (2)$$

2. U-Turn Coupler :

$$Prop_R = \frac{l_{tot}}{l_R} \approx 0.37 \quad (3)$$

We therefore expect mode shapes resembling images (a) and (b) in fig. 47 for the linear and U-turn couplers respectively.

We will not consider this approach and modeling for the sigmoid coupler since its geometry differs too much from the other 2 MEMS devices.

4.1.2 Electromagnetic modeling of the waveguides

4.1.2.1 Waveguide types

In the design of the waveguides we work with waveguides that operate in the near IR range of [1460, 1580] nm, in the TE-00 mode. The waveguides we use are built on an SOI wafer, where *Si* is used as the waveguide medium, with air as cladding, and *SiO*₂ as the buried oxide material. A schematic representation is shown below.

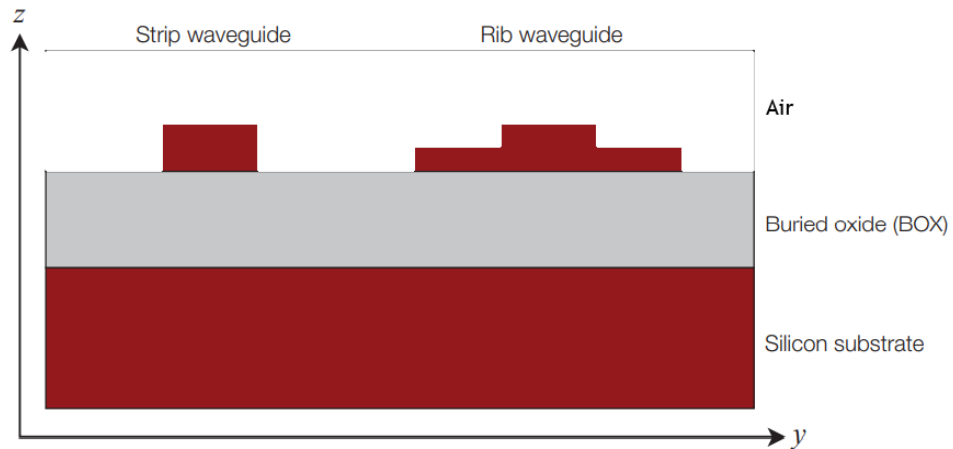


Figure 20: Waveguide material stack. [13]

We use 2 types of waveguides : the strip waveguide (or ridge waveguide), and the rib waveguide, as seen in the picture below.

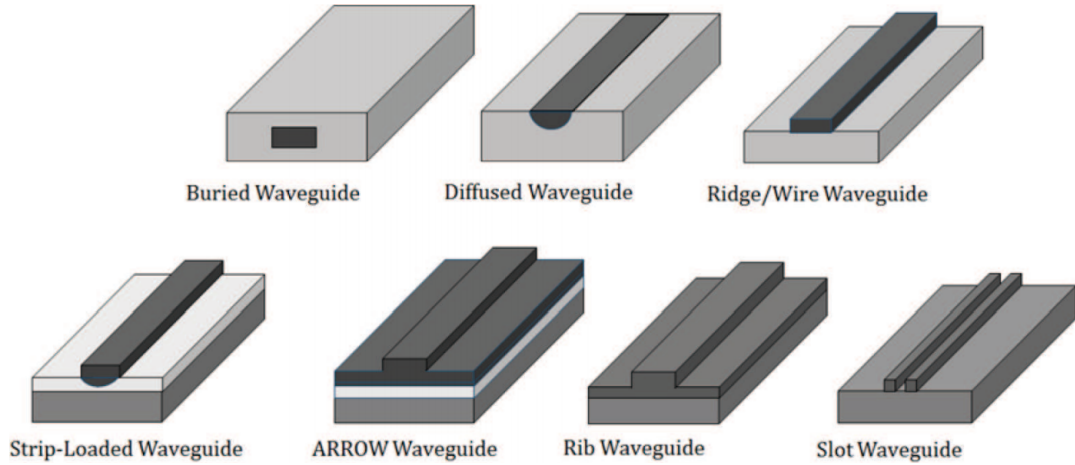


Figure 21: Different types of waveguides. [13]

There are distinct advantages to each waveguide type :

- The strip waveguide is usually used for routing in small spaces, and for PICs, as it offers tight bend radii.
- The rib waveguide is used for active devices such as modulators, since it allows for electrical connections to be made to the waveguide.

4.1.2.2 Mode propagation

Waveguides typically are designed to carry a single mode of the electromagnetic wave we're working with. The main method by which we can limit the number of modes that can be carried by a waveguide is by limiting the geometry. Indeed by modifying either the slab size, or the waveguide width, we can limit the modes that are guided within the waveguides. Since we work with a standardized 220 [nm] thick silicon-on-insulator wafers with 3 [μm] thick buried oxide layers, it is only relevant for us to look at the influence of the waveguide width. According to [14], we can see the influence on the waveguide width in the existence of guided modes, represented in fig. 22.

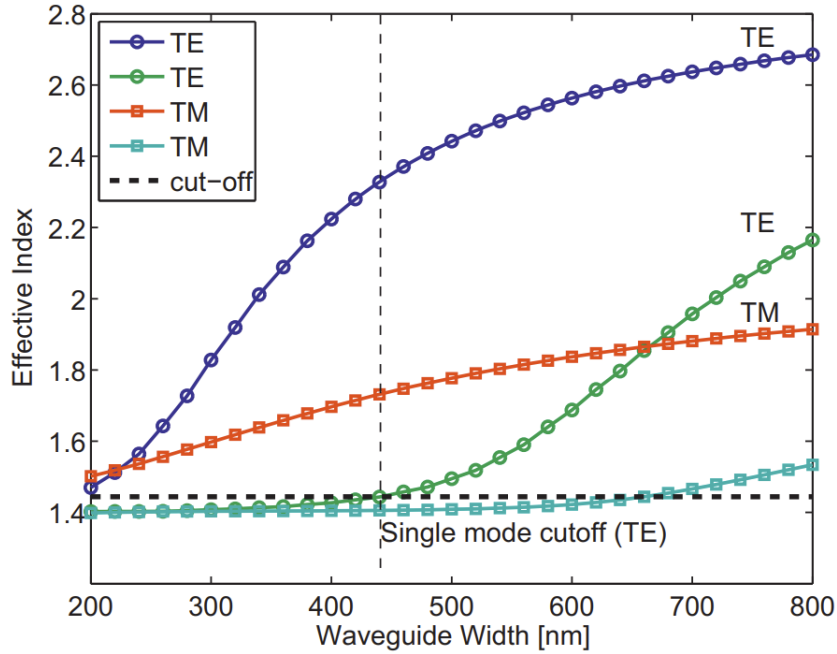


Figure 22: Guided mode existence and dependence on waveguide width, in a 220 nm tall strip waveguide at 1550 nm wavelength. Only the modes above the dotted line exist. [14]

According to the literature : “To obtain a single TE-like mode polarization at 1550 nm, a strip waveguide with a height of 220 nm, and width of 440 nm is required. In this case, the waveguide supports one TE-like and one TM-like mode. For wider waveguides, a second TE-like mode is present, and above 660 nm, a second TM-like mode appears.” [14] It is important to note that such a waveguide does not have a pure TE mode, but rather a combination of the TE and TM modes.

We can also numerically simulate the guided mode shape within the waveguides, and visually make out the geometrical dependence on the existence of multiple guided modes within a waveguide. From literature we can expose the following results :

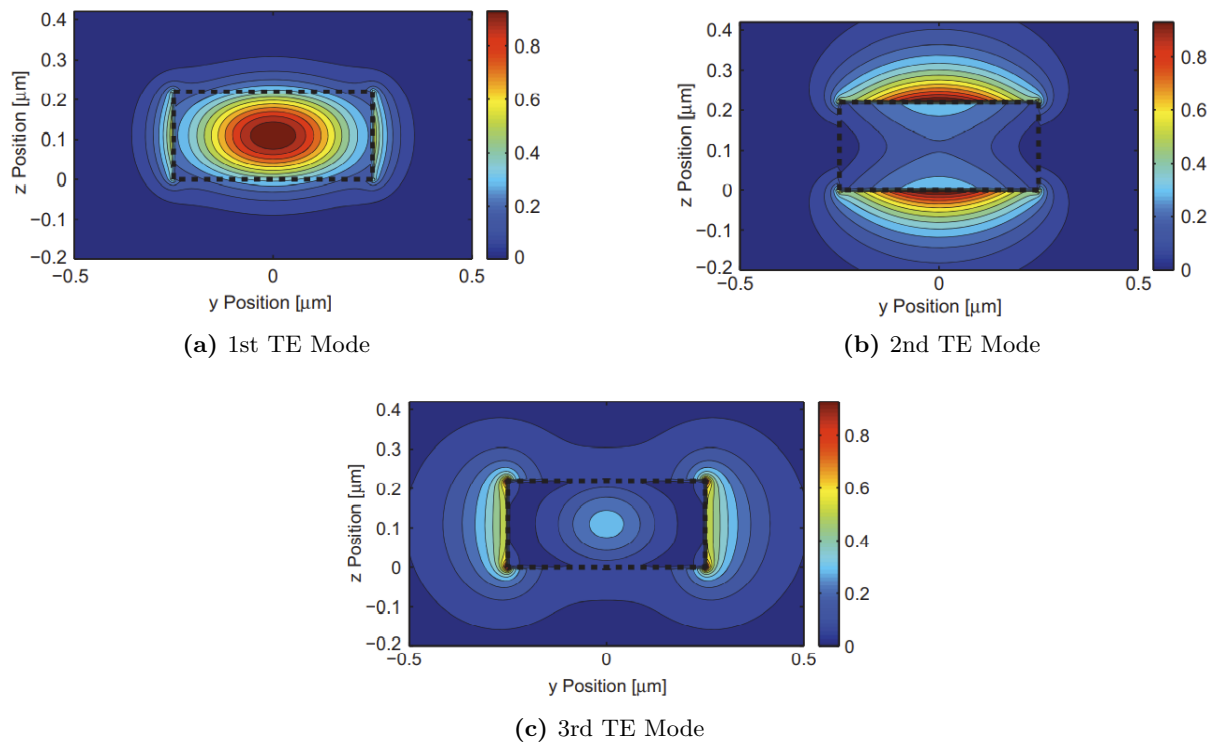


Figure 23: E-Field intensity in a 220×500 [nm] strip waveguide at 1550 [nm]. [14]

4.1.2.3 Waveguide losses

Losses in waveguides come from certain parameters of the geometry and the materials used to fabricate them.

- Sidewall scattering losses. Since the sidewalls are not completely flat and exhibit a certain roughness, they contribute to scattering losses of the guided wave. Typically 2–3 dB/cm for 500×220 nm waveguides.
 - Metal in proximity to the waveguide. Metal absorbs the electromagnetic energy carried by the wave, especially if the guided mode is not perfectly contained within the waveguide. A 500×220 nm strip waveguide with metal above was measured to have an excess loss of 1.8 ± 0.2 dB/cm for metal that is 600 nm above the waveguide.
 - Material losses (mostly prevalent for doped silicon, or polycrystalline silicon).
 - Surface-state absorption can also contribute to the propagation loss if the waveguides are not properly passivated.
 - Sidewall roughness. It can introduce reflections along the waveguide and phase perturbations that are wavelength dependent.

In general, waveguide optical losses can be reduced by using wider waveguides, although as we have explored before, a wider waveguide introduces multiple guided modes within the same waveguide and therefore it is important to be aware of that. One way of dealing with the problem of using wide wavelengths in single-mode, is to create a smooth transition taper between a narrow waveguide and a wide waveguide.

This loss modes are take into account for the analysis of straight waveguides, as bends introduce other types of loss mechanisms.

4.1.2.4 Bent waveguide losses

Losses in bent waveguides can, originate from all the loss mechanisms we exposed in paragraph 4.1.2.3. However we do need to take into account the radiative losses, especially since we are working with highly confined tight bends. Other mechanisms such as scattering losses and substrate leakage are small.

The largest source of losses in bends in waveguides comes from mode mismatching. It originates from the imperfect mode overlap when transitioning from a straight waveguide into a bent waveguide. This mismatch leads to scattering losses at the interface at which the curvature changes discontinuously.

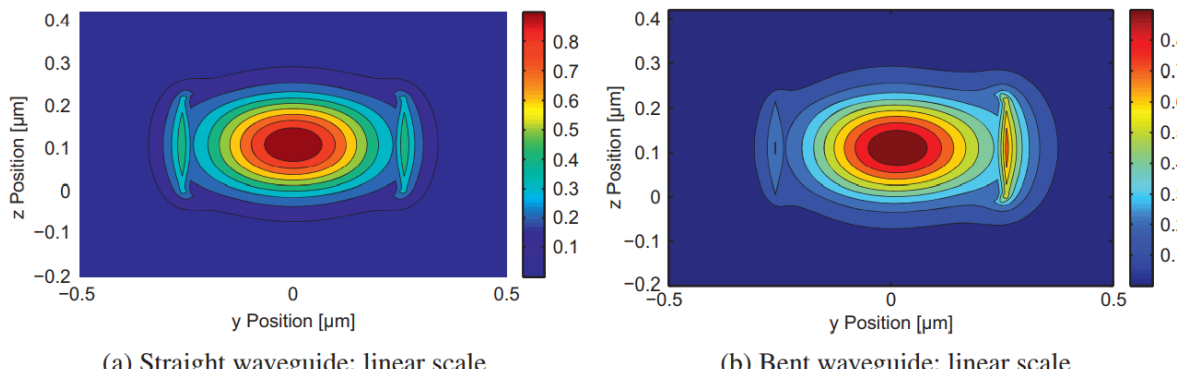


Figure 24: Electric field mode profile for a 220×500 [nm] strip waveguide at 1550 [nm]. (a) : Straight waveguide. (b) : Bent waveguide at 2 [μm] curvature radius. [14]

There are 2 main methods that can be used to mitigate this loss mechanism :

1. Increase the mode overlap : the fraction of the power transmitted into the bend mode. This is mostly done by simulating the overlap if no correction is done (manually computing this is usually not done because of the mathematical complexity), and then physically shifting the waveguide such that the modes overlap.

2. Create a waveguide for which the curvature varies continuously, thus maintaining an ideal mode overlap between each curve element dS .

In our designs we use the second method extensively, using sine-circle-sine curve matching, as well as tapering sections to transition from strip to rib waveguide sections and vice-versa. This method was developed by W. Bogaerts *et al.*, and consists of a rib to strip taper, followed by a curve matched bend at a waveguide width of 450 [nm] [6] [5]. This enables the use of really tight bends at low radii of curvature, yet maintaining acceptable losses.

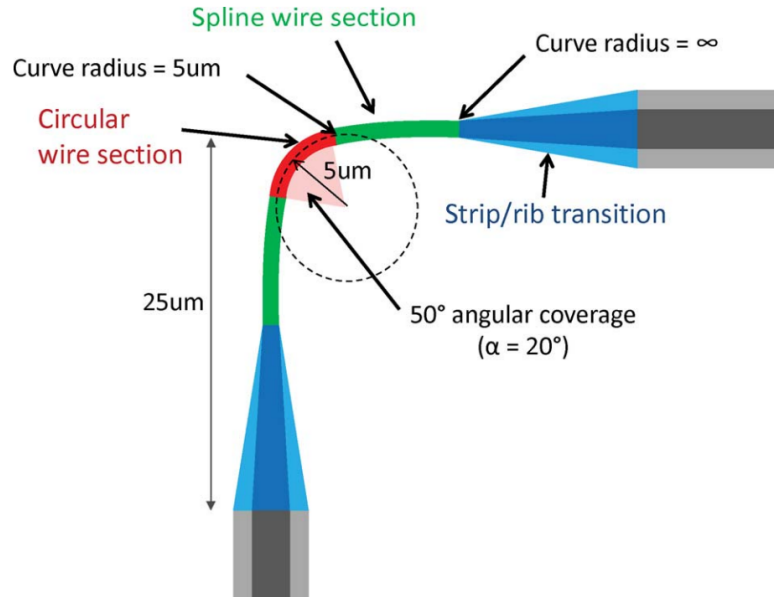


Figure 25: Hybrid rib/strip curve matched bend example, as developed by W. Bogaerts *et al.* [6]

For strip and rib waveguides, the losses found in literature for a 90° bend as a function of bend radius are given below [14] :

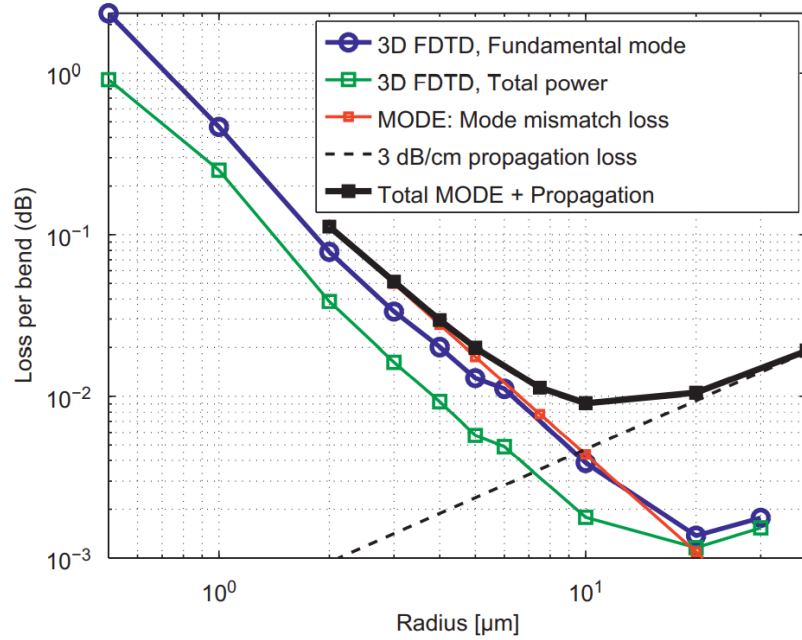


Figure 26: Optical losses per 90° bend for a 220 × 500 [nm] strip waveguide at 1550 [nm] as a function of bend radius. [14]

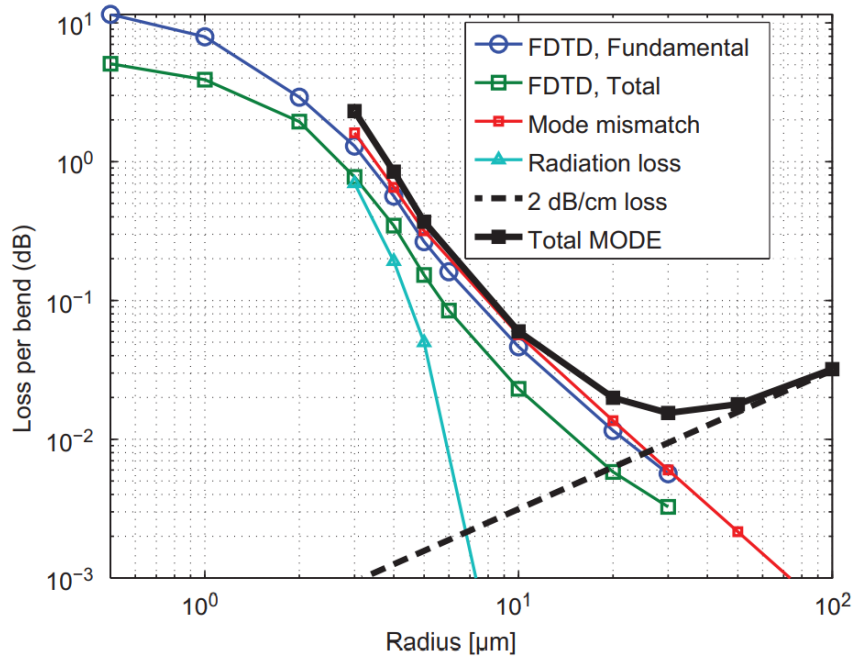


Figure 27: Optical losses per 90° bend for a 220 × 500 [nm] rib waveguide at 1550 [nm] as a function of bend radius. [14]

4.2 Computation of optical losses

We use a simple model based on the research papers previously discussed. Since the optical losses are highly dependent on the surface roughness, which in itself is related to the fabrication methods which vary widely depending on the foundry used for the wafer fabrication, and we do not have access to the exact parameters required for a precise computation, we will use the data from literature [14], and from previous research by Dr. Furci.

Therefore we find the following required parameters for the computation of the optical losses :

- Propagation loss : $L_{Prop} = 1.6 \text{ [dB/cm]}$, obtained from research done by Dr. Furci.
- Bend loss, for a 90° bend at a radius of 5 [\mu m] , for a strip waveguide : $L_{bend, r=5} = 2 \times 10^{-2} \text{ [dB/bend]}$, from fig. 26
- Bend loss, for a 90° bend at a radius of 8 [\mu m] , for a strip waveguide : $L_{bend, r=8} = 1 \times 10^{-2} \text{ [dB/bend]}$, from fig. 26
- Low loss crossing loss : $L_{LLC} = 0.011 \text{ [dB/crossing]}$, from previous research [4].

When computing the optical losses for a bend, as we mentioned previously, there are multiple contributions to take into account : the propagation losses, radiation losses, scattering losses, etc. Referring back to fig. 26 and fig. 27, we will use the black curves referred to as “Total MODE”, which represent the addition of all losses originating from bends and the propagation loss as described in paragraph 4.1.2.3. Thus for bends smaller than approx. 12 [\mu m] for strip waveguides, and smaller than approx. 16 [\mu m] for rib waveguides, the bend losses dominate and we can simply use the aforementioned graphs as look up tables.

Therefore, for bends smaller or larger than 90° , we simply multiply the $L_{bend} \times l_{bend}$ factor by a scale factor that allows us to match the bend to the baseline value of a 90° bend that we find in the literature. For example : if we compute the loss for a 45° bend, we simply compute : $L_{bend} \times l_{bend} \times \frac{1}{2}$. We chose the original direction of light propagation before the bend as the reference for the 0° angle.

We combine these parameters in a simple computation where we consider only straight segments and curved segments, computing for each curvature radius value as such :

$$L_{Total} = l_{straight} \cdot L_{Prop} + s_{(curve, r_i)} \cdot L_{(bend, r=r_i)} + L_{LLC} \quad (4)$$

Where L_{foo} represents the optical loss, l_{foo} represents the length, and s_{foo} is the scale factor.

We compute the optical losses for the 3 chosen designs and obtain the following results :

	Linear Design	U-Turn Design	Sigmoid Design
Estimated losses for the BWG [dB]	0.0595	0.1344	0.0845
Estimated losses for the coupler [dB]	0.0167	0.0496	0.0698

Table 1: Estimated optical losses for the 3 designs.

Note that for the coupler losses we did **not** include the estimated switching loss of 0.47 [dB/switch] obtained from research [3], and only consider the losses intrinsic to the waveguide on the coupler. The main result that we can extract from this computations is that the U-Turn design exhibits an excessive attenuation of the optical signal, as the loss per cell is 0.1344 [dB]. This is about 5 times higher than the optical losses reported by the researchers who developed the original design [4].

It is nonetheless important to clarify that these computations are not precise, but give us a good idea of the order of magnitude of the optical losses we can expect. A more precise result could be obtained by simulating the entire structure using finite element methods, but this characterization is out of the scope of the project.

4.3 Simulations on COMSOL Multiphysics®

4.3.1 Buckling mode shape analysis

We performed COMSOL simulations to identify the first mode shapes of each of the design's couplers. These simulations use the linear buckling preset from COMSOL which performs a 2-step study [11]:

1. A stationary study step during which the software applies a given external load on the structure as defined by the boundary conditions.
2. A linear buckling step, in which an eigenvalue solver is used to compute the buckling eigenmodes (buckling mode shapes) at each of the load factors.

The output given by the simulation is the mode shape of the structure, and the critical load factor for each mode shape.

To better understand the meaning of this load factor is by considering the following equation :

$$(K_L + K_{NL})\mathbf{u} = \mathbf{f} \quad (5)$$

Where, K_L and K_{NL} are the linear and non linear stiffness matrices respectively, \mathbf{u} is the displacement vector, and \mathbf{f} is the stationary load applied on the structure.

The solver first solves the problem for an initial load \mathbf{f}_0 , and finds a solution \mathbf{u}_0 for the linear problem. Then, the non-linear problem is approximated as such :

$$(K_L + \lambda K_{NL}(\mathbf{u}_0))\mathbf{u} = \lambda \mathbf{f}_0 \quad (6)$$

We call λ the load multiplier. The displacement \mathbf{u} therefore goes to infinity (and we thus reach buckling), when the left-hand side of the equation tends to 0. The value of the load multiplier for which this condition is true is found through the second study step.

The output “critical load factor” as given by COMSOL is therefore the value of λ for which this buckling instability is reached. If the initial load actually was larger than the buckling load, then the critical value of λ is smaller than 1.

For the simulations we performed, we applied a compressive stress value of :

$$S_{critical} = 7.7867 \times 10^6 \text{ [Pa]} \quad (7)$$

And a vertical load of :

$$F_z = 2.7253 \times 10^{-10} \text{ [N]} \quad (8)$$

These values are based on previous simulations performed on the original design, by Dr. Furci.

The critical load factor obtained is therefore the λ multiplier on the initial load of F_z .

4.3.1.1 Linear Coupler

We present the first 3 mode shapes of the linear coupler under buckling.

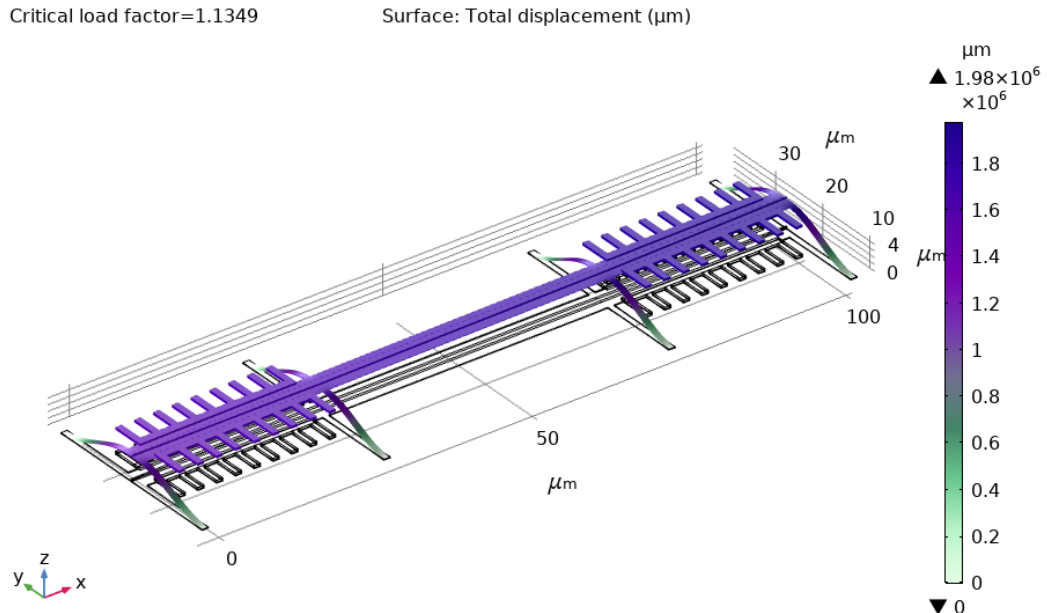


Figure 28: 1st buckling mode shape for the linear coupler. $\lambda = 1.135$

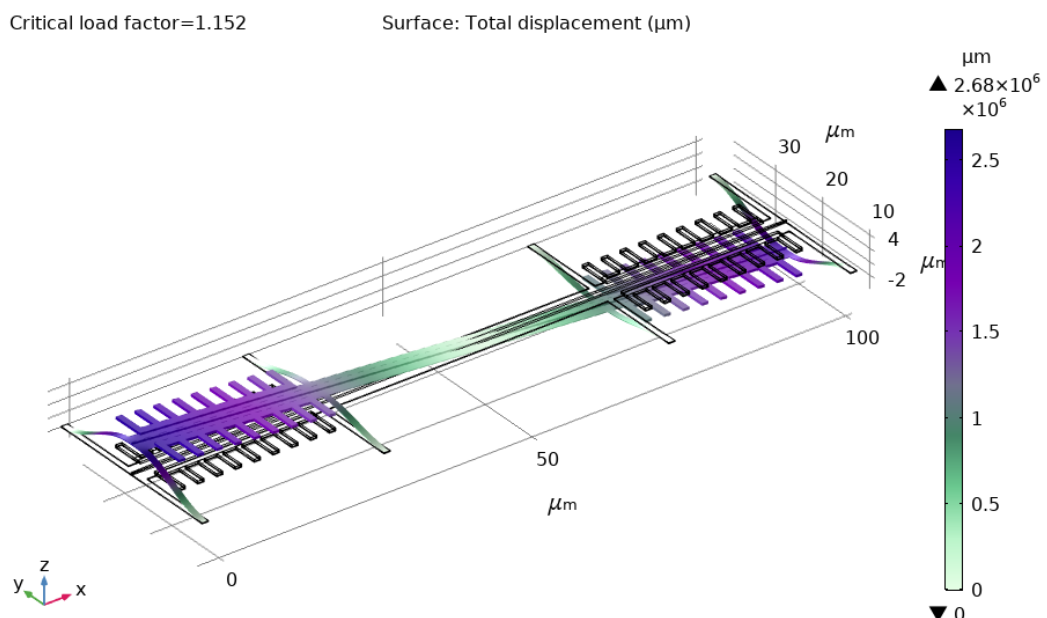


Figure 29: 2nd buckling mode shape for the linear coupler. $\lambda = 1.152$

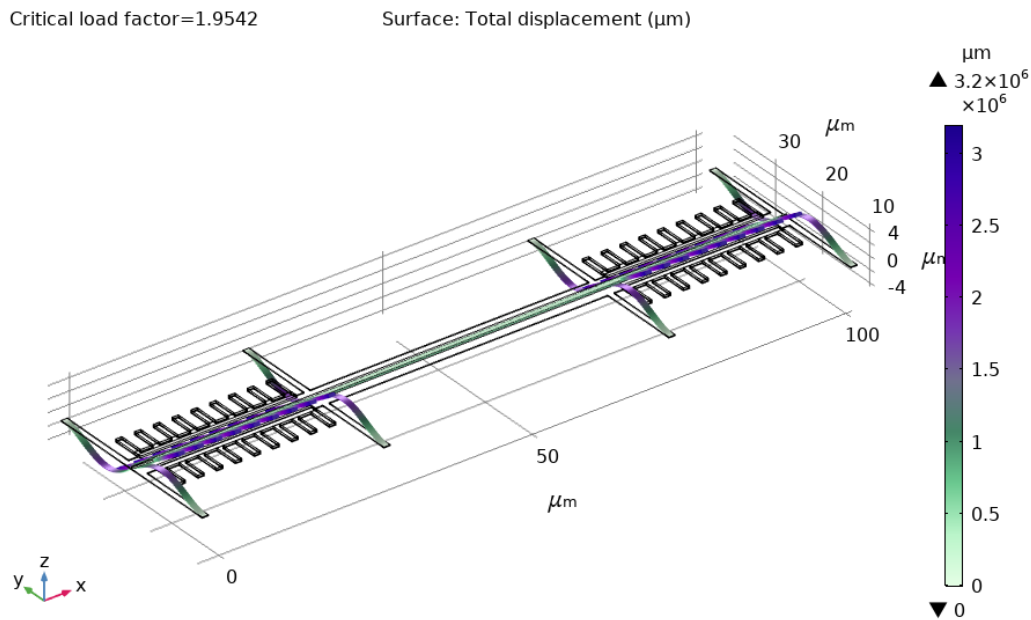


Figure 30: 3rd buckling mode shape for the linear coupler. $\lambda = 1.954$

4.3.1.2 U-Turn Coupler

We present the first 3 mode shapes of the U-Turn coupler under buckling.

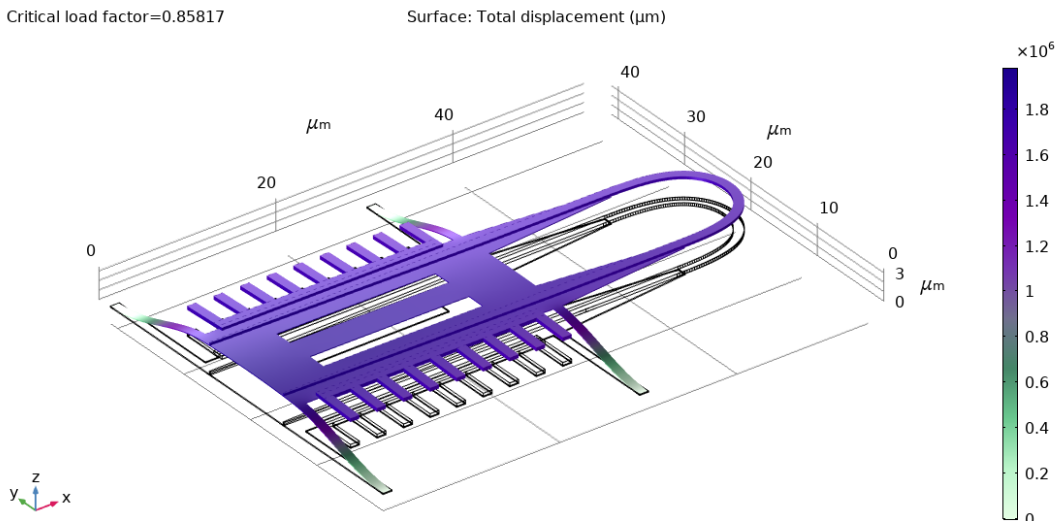


Figure 31: 1st buckling mode shape for the U-Turn coupler. $\lambda = 0.858$

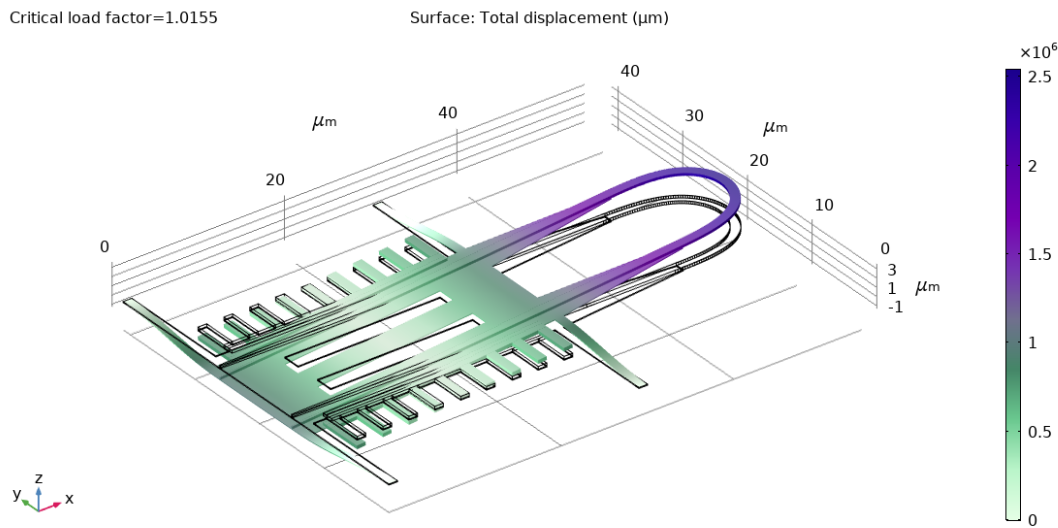


Figure 32: 2nd buckling mode shape for the U-Turn coupler. $\lambda = 1.016$

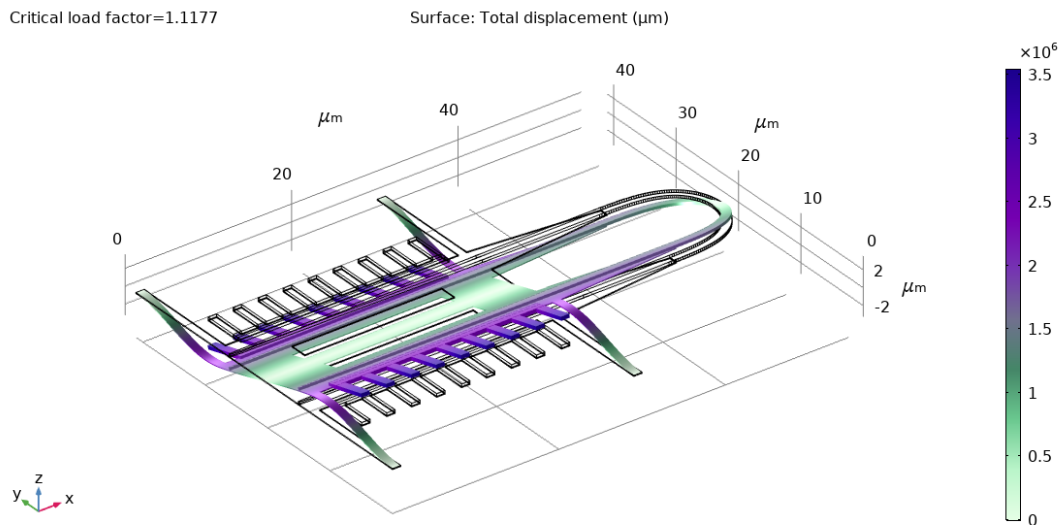


Figure 33: 3rd buckling mode shape for the U-Turn coupler. $\lambda = 1.118$

4.3.1.3 Sigmoid Coupler

We present the first 3 mode shapes of the sigmoid coupler under buckling.

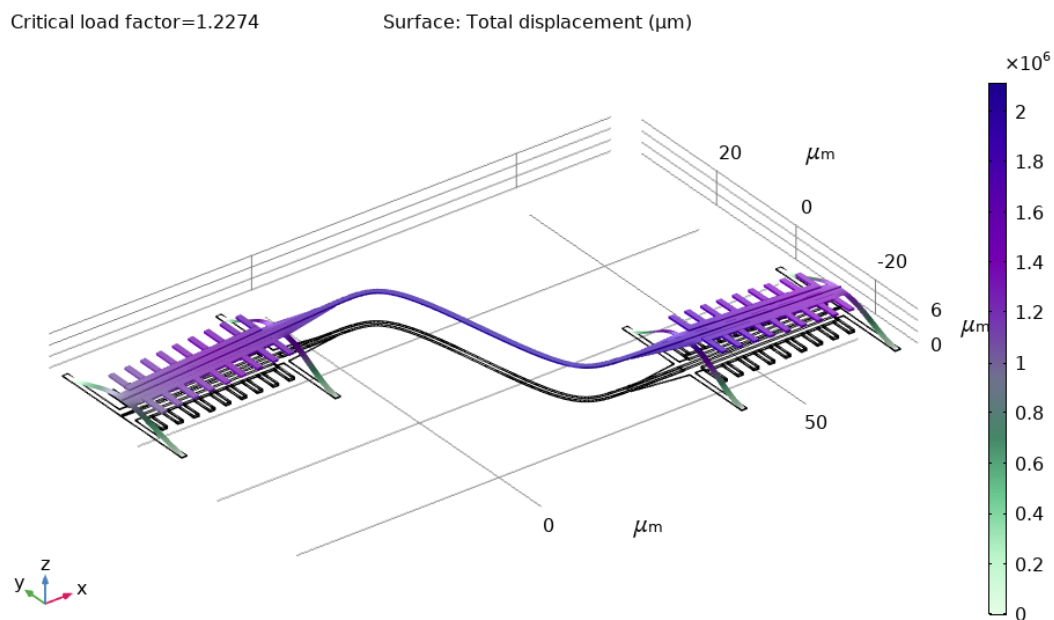


Figure 34: 1st buckling mode shape for the Sigmoid coupler. $\lambda = 1.227$

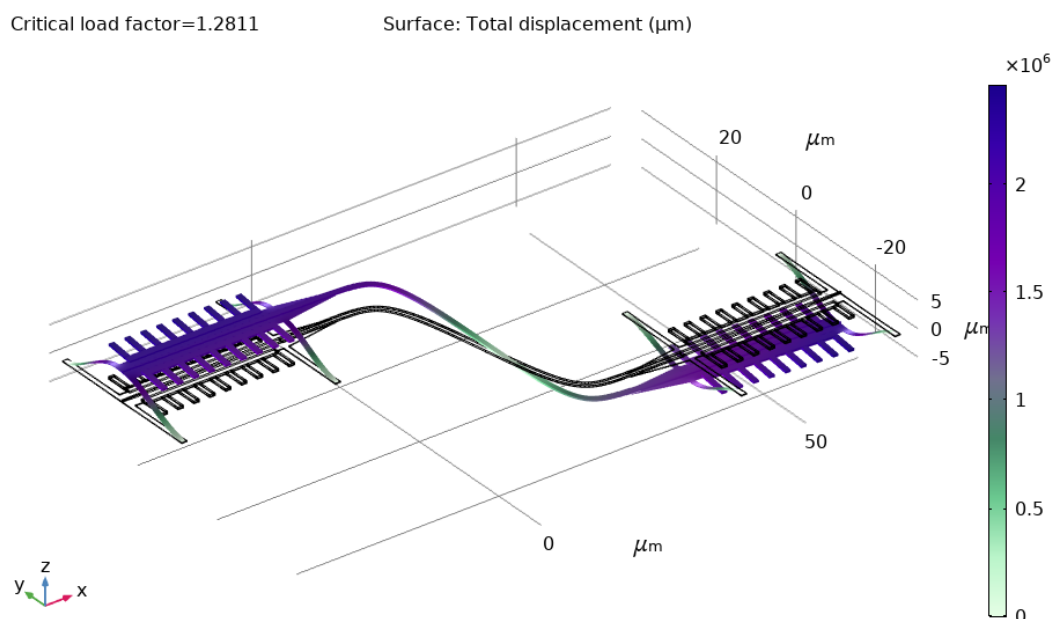


Figure 35: 2nd buckling mode shape for the Sigmoid coupler. $\lambda = 1.281$

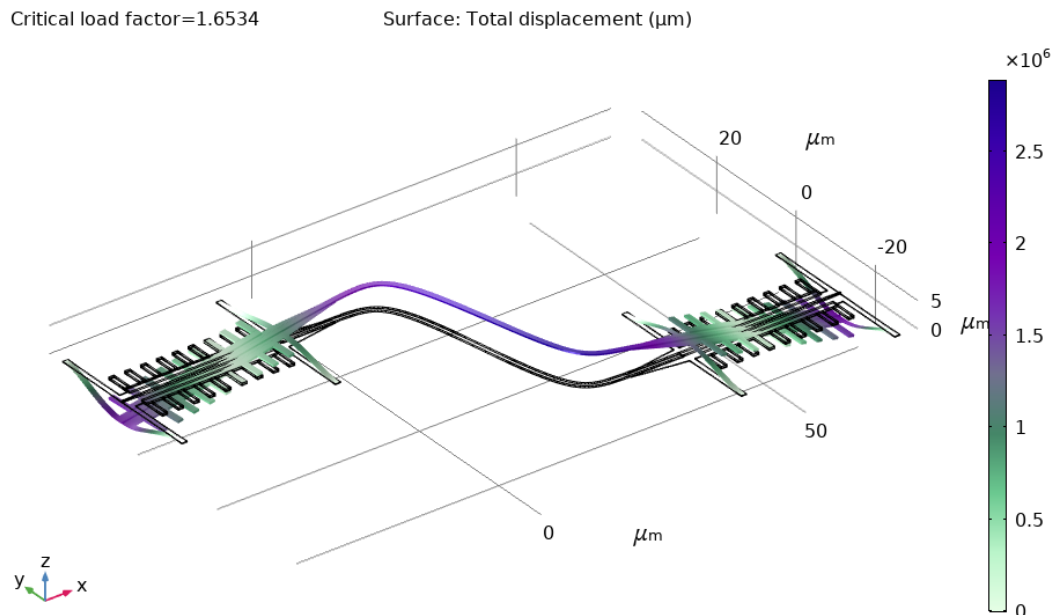


Figure 36: 3rd buckling mode shape for the Sigmoid coupler. $\lambda = 1.653$

4.3.2 Estimation of the deflection

We estimate the deflection of each coupler, as a first qualitative approach aimed at ensuring that the displacement of the coupler is enough to enable coupling between the top and bottom layers.

We performed a stationary study, for which we take into account the same parameters from eq. (7), and eq. (8). We then provide the results as the displacement field in the vertical z direction for each structure.

4.3.2.1 Linear Coupler

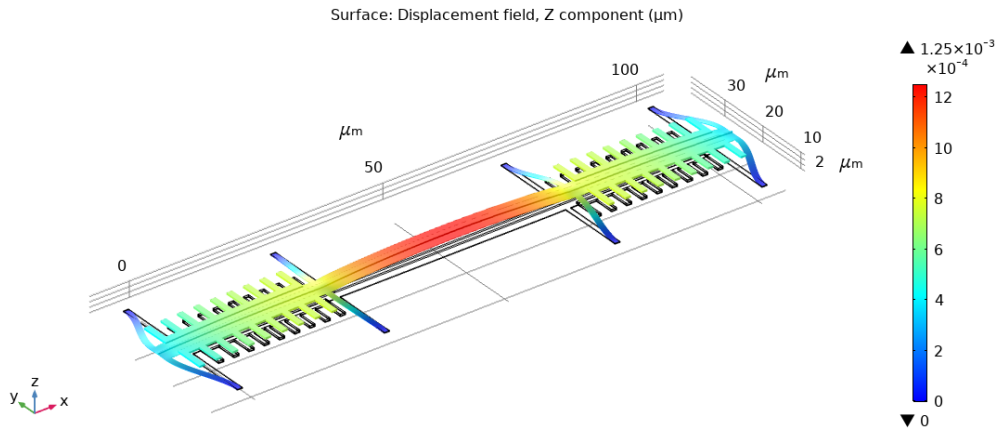


Figure 37: Vertical displacement of the linear MEMS coupler.

It is interesting to note in fig. 37, that as the coupler buckles up, it also bends the suspension arms in the linear x direction (according to the axis on the same figure) of the coupler as the arms try to minimize the internal stress. This induces a displacement in that same direction possibly changing the overlap distance between the adiabatic couplers in the top and bottom waveguides.

4.3.2.2 U-Turn Coupler

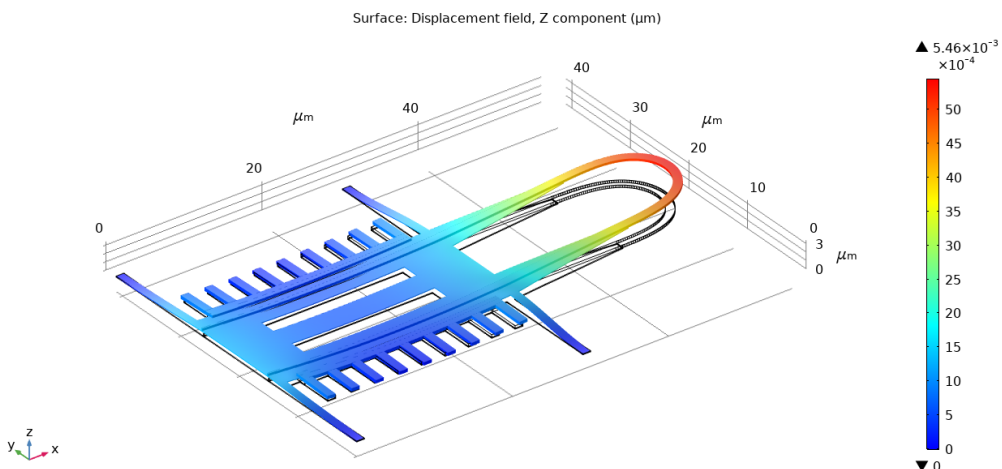


Figure 38: Vertical displacement of the U-turn MEMS coupler.

We can observe in fig. 38 that keeping the same actuation parameters as mentioned previously, the added mass of the membrane, and the fact that we removed 2 comb actuators means that the system does not deflect as much as required, and in fact according to the simulation, it deflects by around 1 [nm]. This might be an indication that it is required to increase the actuation force, or potentially re-modify the MEMS in order to add a comb drive actuator in the middle, sacrificing footprint for actuation force.

We performed a parameter sweep on the actuation load using the COMSOL sweep setting, and found that applying a load 100 times larger we obtain deflection of 150 [nm], according to the simulation.

4.3.2.3 Sigmoid Coupler

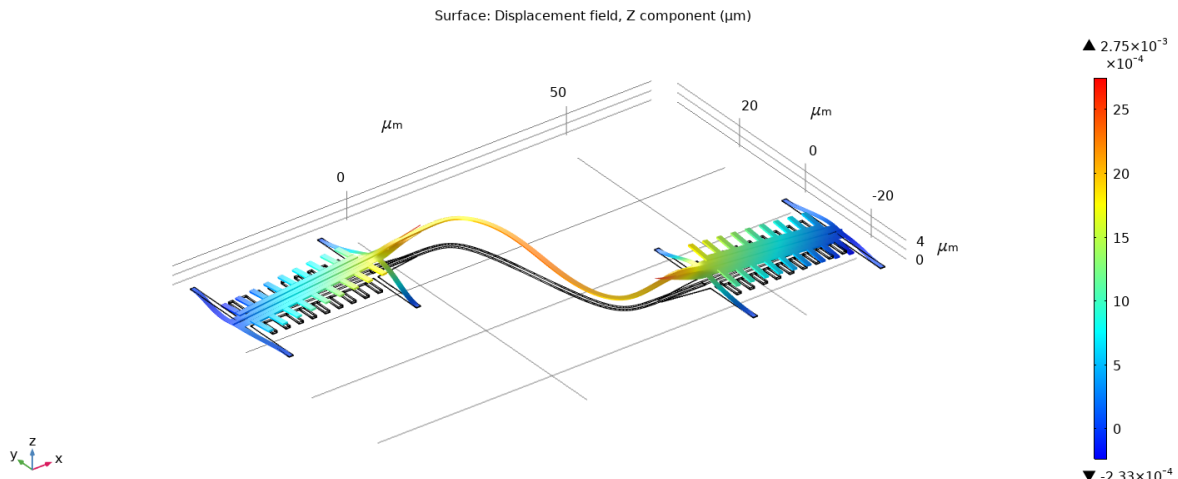


Figure 39: Vertical displacement of the sigmoid MEMS coupler.

The sigmoid coupler shows the biggest deflection in the middle suspended part of the coupler, which is normal since it is the lightest and also is mechanically unstable, as we predicted. The tapering to transition between rib and strip waveguides created an artifact in the simulation as it appears to have been broken, despite being part of the same component in the **Geometry** parameters within COMSOL. In the inlet and outlet of the coupler, the device dips down. The total deflection is in fact quite small, which is most likely due to the higher mass of the coupler, and its large size.

4.3.3 Estimation of the effective stiffness of the couplers

We estimate the effective stiffness of each coupler by computing its eigenfrequency using the COMSOL *Prestressed eigenfrequency* study. It is used to compute eigenfrequencies and eigenmodes that are influenced by a prior static load. The study consists of two study steps: a *Stationary study step* followed by an *Eigenfrequency study step*. The study computes the eigenfrequencies and the shapes of the eigenmodes when influenced by a prior static load on the structure.

We can then estimate the effective stiffness as follows :

$$f_0 = \frac{1}{2\pi} \sqrt{\frac{k_{eff}}{m}} \quad (9)$$

$$\implies k_{eff} = (2\pi f_0)^2 \cdot m \quad (10)$$

4.3.4 Results

The results are summarized in the tables below :

	Linear Coupler	U-Turn Coupler	Sigmoid Coupler
λ : 1st mode	1.135	0.858	1.227
λ : 2nd mode	1.152	1.016	1.281
λ : 3rd mode	1.954	1.118	1.653

Table 2: Summary of the critical load factors λ for each coupler, for the first 3 buckling mode shapes.

	Linear Coupler	U-Turn Coupler	Sigmoid Coupler
Eigenfrequency [Hz]	62.625×10^3	61.535×10^3	78.154×10^3
Mass [kg]	4.1407×10^{-13}	2.985×10^{-13}	4.00×10^{-13}
Effective stiffness [$kg \cdot s^{-2}$]	0.06	0.04	0.09

Table 3: Derived mechanical parameters of the couplers, as simulated by COMSOL.

From these results we can conclude that without changing the fabrication methods used and described in previous research [4], and for the same initial loads applied by the comb drive actuator, the U-Turn design is the most viable since its λ factor is lower than 1.

A problem that arises as well is that the λ factor for the first 2 modes of the sigmoid coupler and the linear coupler are quite close to each other, meaning that if the load applied is not precisely controlled the second, unwanted mode could be excited and potentially malfunction.

5 Limitations and discussion

5.1 Design limitations

The main limitation regarding the design of the unit cells is the low-loss crossing. In fact for all 3 designs proposed in this research, we reach a point in which the MEMS coupler is as miniaturized as possible for each design, and reach the dimensions of the coupler. The problem now becomes the fact that the dimensions of the low-loss crossing cannot be altered, as it is made so that the crosstalk between the through and drop channels is minimal. Modifying the dimensions would inevitably increase the cross-talk, and compromise the functionality of the array.

Therefore, it is worth contemplating a solution in which the low-loss crossing is modified, either by reducing the overall size, or by adapting the geometry so that the branches meet each other at an angle for examples.

This goes hand-in-hand with the second limitation of the design, which is the requirement for extremely low optical losses per unit cell. Indeed, any unit cell design for which the optical loss is comparable to the low-loss crossing itself is likely to be excessive for the particular applications we're aiming for. Indeed, referring back to table 1 we can see that the lowest losses in the BWG for all of our designs, achieved for the linear coupler design, is already about 5 times higher than the losses recorded for the low-loss crossing. For the most compact design, we obtain losses 10 times higher for the unit cell than for the low-loss crossing. Unfortunately, this means that despite being quite compact, the U-Turn design is most likely not viable. From these results we see that in order to miniaturize the design, so as to reach the dimensions of the low-loss crossing, we must introduce extremely tight bends, at radii of 5 [μm] at the lowest, which introduces high losses.

5.2 Software limitations

The main limitations in term of design pipeline come from the poor quality of the softwares used for the design of MEMS.

There is no integrated, universal MEMS design software platform that we are aware of, and therefore we must software suits that were designed for the fabrication of IC components in the microelectronics industry such as L-Edit. The software is behind a paywall, and access to documentation is extremely limited. There are no official forums, the available documentation online is outdated, and overall the software is outdated and is not pleasant to use. Moving back and forth between other CAD softwares such as Autodesk Inventor, or Catia V5 and L-Edit shows the limitations in regards of user interface customization, keybinding customization

and default keybinds and controls, and overall standardization with the rest of CAD softwares used in the engineering design industry. Simple things such as exporting or importing masks, converting a `.tdb` file to `GDS` and other such actions are unnecessarily complex, mostly due to the proprietary aspect of L-Edit's software.

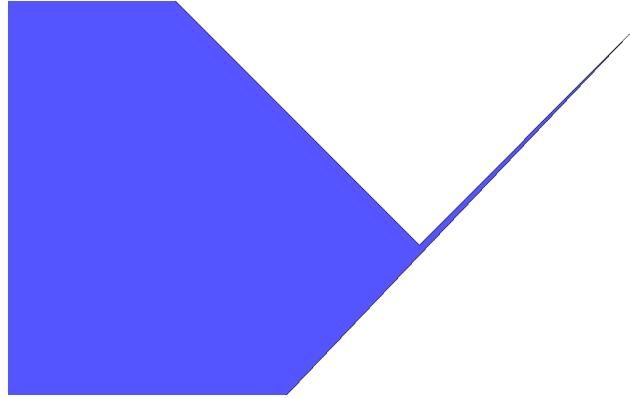


Figure 40: L-Edit artifact in one of the Sine-Circle-Sine modules

L-Edit also does not deal well with any geometric entity that is not perfectly aligned with the underlying grid. Importing the modules to build the Sine-Circle-Sine BWG as mentioned in section 3.2 was overly complicated as the geometry would be corrupted, and artifacts would be created in the geometry. Opening the same files on another software such as K-Layout yields a perfect result in terms of geometry, and this facts leads us to question the efficacy of L-Edit when designing MEMS structures that are often much more complex than what L-Edit allows users to do.

6 Conclusions and future prospects

In this research paper, we presented 3 optimized optical MEMS switch architectures, in the aim of improving the mechanical stability of the MEMS coupler by exploiting uniaxial residual stress only, decreasing the overall footprint, maintaining low optical losses, and improving the switching speed.

3 designs were proposed, each one with a different geometry design for the coupler : linear, u-turn and sigmoid shapes were explored. After optimizing the geometry of all designs as much as we could, all of them respected our constraints of **uniaxial stress, and footprint reduction**. These two aspects were attainable within the original design structure. The footprint reduction was not as effective as was hoped at the onset of the project, since we reached a point where the limiting element in terms of footprint was the multimode low-loss crossing, that we could not modify. To that extent it seems difficult to improve the footprint further without also modifying somewhat the design of the crossing.

As for the **optical losses**, it became clear that in order to miniaturize the MEMS and the overall footprint of the unit cell, we needed to introduce tight curves in the bottom waveguide, which in turn introduced high optical losses. We were not able to obtain losses comparable to the original design's. The switching speed was not estimated, and only an estimation of the effective stiffness of each coupler was computed. The characterization of this parameter would require a dynamical simulation followed by an on-chip characterization, which were out of the scope of the project.

We conclude by stating that, with the exception of the sigmoid coupler which would be more effective at a smaller scale, the couplers proposed are effective solutions for micrometer-sized latching broadband optical coupling switches in general. Applications where higher optical losses are acceptable, and low energy consumption is a requirement, such as low channel count switching PICs, or similar, would be the best suited for this type of approach. As for high channel count switch arrays as the one proposed in this paper, the introduction of multiple tight bends in order to miniaturize the unit cell's size, along with the bulky geometry of the low-loss crossing are the main limiting parameters.

I would like to thank my supervisor, Dr. Hernán Furci whose expertise was of paramount importance for the development of the solutions proposed in this paper, for his advice and for the insightful discussions that we had in the context of the project and other such themes.

I would like to thank Prof. Dr. Niels Quack for his creative ideas, his support in the development of the project, for all the theoretical knowledge that was kindly taught throughout the duration of the project, and for opening up my future research prospects and goals in the field of photonics.

References

- [1] Trey Roessig, “Mirrors with Integrated Position Sense Electronics for Optical-Switching Applications | Analog Devices”, October 2010.
- [2] Baojun Li, Ed., *Optical switches: materials and design*, Woodhead publishing in materials. Woodhead, Cambridge, 2010, OCLC: 700407249.
- [3] Tae Joon Seok, Niels Quack, Sangyoon Han, Richard S. Muller, and Ming C. Wu, “Large-scale broadband digital silicon photonic switches with vertical adiabatic couplers”, *Optica*, vol. 3, no. 1, pp. 64–70, January 2016, Publisher: OSA.
- [4] Hamed Sattari, Adrien Toros, Teodoro Graziosi, and Niels Quack, “Bistable silicon photonic MEMS switches”, in *MOEMS and Miniaturized Systems XVIII*, Wibool Piyawattanametha, Yong-Hwa Park, and Hans Zappe, Eds. 2019, vol. 10931, pp. 97 – 104, SPIE, Backup Publisher: International Society for Optics and Photonics.
- [5] Wim Bogaerts, Pieters Dumon, Dries Van Thourhout, and Roel Baets, “Low-loss, low-cross-talk crossings for silicon-on-insulator nanophotonic waveguides”, *OPTICS LETTERS*, vol. 32, no. 19, October 2007.
- [6] Wim Bogaerts and Shankar Kumar Selvaraja, “Compact Single-Mode Silicon Hybrid Rib/Strip Waveguide With Adiabatic Bends”, *IEEE Photonics Journal*, vol. 3, no. 3, pp. 12, March 2011.
- [7] Minh Tran, Duanni Huang, Tin Komljenovic, Jonathan Peters, Aditya Malik, and John Bowers, “Ultra-Low-Loss Silicon Waveguides for Heterogeneously Integrated Silicon/III-V Photonics”, *Applied Sciences*, vol. 8, no. 7, pp. 1139, July 2018.
- [8] The MathWorks Inc., “MATLAB”, 2021.
- [9] Tanner Tools, “L-Edit IC”, 2016.
- [10] Matthias Köfferlein, “KLayout”, 2021.
- [11] COMSOL AB, “COMSOL Multiphysics®”, 2021.
- [12] K Baker, “The Mathematics of Computer Graphics”, *University of California, Los Angeles (UCLA)*, vol. 1, no. 1, pp. 21, 2003.
- [13] Shankar Kumar Selvaraja and Purnima Sethi, “Review on Optical Waveguides”, in *Emerging Waveguide Technology*, Kok Yeow You, Ed. InTech, August 2018.
- [14] Lukas Chrostowski and Michael Hochberg, *Silicon Photonics Design*, Cambridge University Press, Cambridge, 2015.
- [15] Jia-Jang Wu, “Use of the elastic-and-rigid-combined beam element for dynamic analysis of a two-dimensional frame with arbitrarily distributed rigid beam segments”, *Applied Mathematical Modelling*, vol. 35, no. 3, pp. 1240–1251, March 2011.

A Relaxed uniform cubic B-spline curve description

This description is based on work done by K. Baker, from the University of California, Los Angeles (UCLA) [12].

In this annex we describe the mathematics of relaxed uniform cubic B-spline curves, referred to as Bézier curves or Bézier splines.

Bézier splines were developed by Pierre Bézier, who used them in the 1960s for designing curves for the bodywork of Renault cars. These curves are related to Bernstein polynomials.

A subset of Bézier splines is the set of cubic spline curves.

Definition : A cubic spline is a piece-wise cubic curve (3rd order polynomial) with a continuous second derivative where it is defined.

Cubic splines are defined by their “control polygons”, which are a set of points ($P_0, P_1, P_2, P_3, \dots$) that describe the Bézier curve $\mathbf{B}(t)$ such that :

$$\mathbf{B}(t) = \sum_{i=0}^n \binom{n}{i} (1-t)^{n-i} \cdot t^i \cdot \mathbf{P}_i \quad (11)$$

Where n is the degree of the polynomial created, and \mathbf{P}_i is the i -th point on the control polygon. For cubic splines, $n = 4$. An example is shown below.

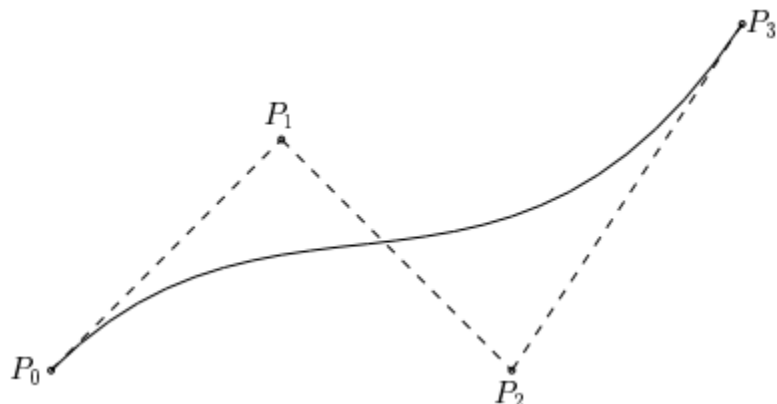


Figure 41: Example of a cubic Bézier curve.

We will see in appendix B that the curvature and curvature radius of a curve is dependent on the second derivative of the function describing the curve. The fact that we are using cubic splines insures that the second derivative is continuous, however we require an additional condition : we need the end points of our curve to have 0 curvature, since we are coupling the element of the BWG described by Bézier curves to a straight section of waveguide.

Let us admit the following : *the curvature of a function at a given point x_0 is zero, if its second derivative is 0 at x_0 .*

Definition : A cubic spline is referred to as *relaxed* if its second derivative is 0 at each end point.

This object is particularly interesting since this means that can use multiple cubic relaxed splines glued to each other, and with different concavity/convexity, in order to match turns that have 0 curvature in the middle. The condition required for a cubic spline to be relaxed is :

$B''(0) = 0$ if and only if P_1 is the midpoint of the segment $\overline{P_0P_2}$. $B''(1) = 0$ if and only if P_2 is the midpoint of the segment $\overline{P_1P_3}$.

A relaxed cubic spline is shown below.

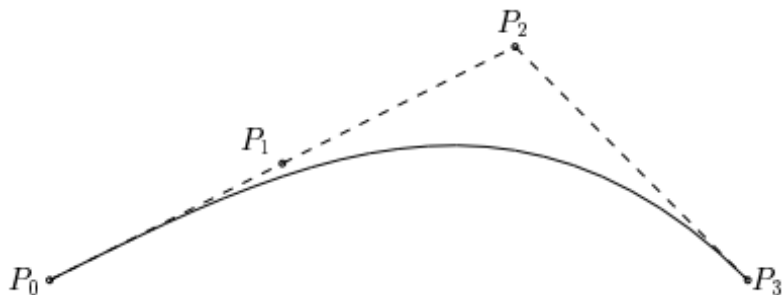


Figure 42: Example of a relaxed cubic Bézier curve.

It is clear, however, that simply matching the end-points of 2 cubic relaxed splines is not sufficient. Simply matching the end points can clearly lead to situations where the first derivative is not continuous over the length of the entire curve, and therefore it is useless for us. In the same manner we also need to match the second derivative, to insure a continuous curvature over the entire length of the function.

For 2 cubic relaxed splines with control polygons (P_0, P_1, P_2, P_3) and (Q_0, Q_1, Q_2, Q_3) , and joined at point S , we can create 2 points A_+ and A_- such that : $A_+ = 2 \cdot P_2 - P_1$ and $A_- = 2 \cdot Q_2 - Q_1$. These are the right and left apexes of the curve, as shown below.

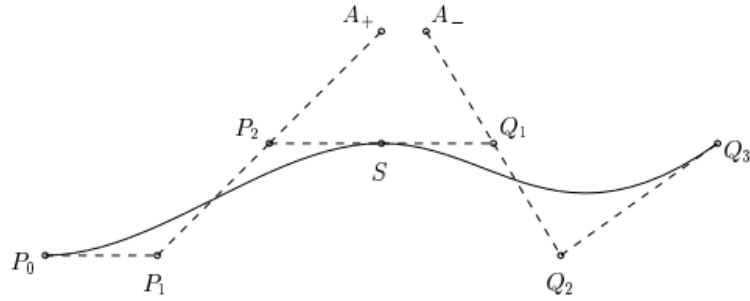


Figure 43: Example of two relaxed cubic Bézier curve glued at point S , apexes shown.

It can be shown that the second derivatives will be continuous over the entire curve (and most importantly at point S), if and only if, $A_+ = A_- = A$. Therefore this means that the second derivatives of 2 joined cubic relaxed B-spline curves match at the joint point S if and only if : S is the midpoint of $\overline{P_2Q_1}$, P_2 is the midpoint of $\overline{P_1A}$, Q_1 is the midpoint of $\overline{Q_2A}$.

These are therefore the conditions that we need to fulfill in order to generate appropriate cubic B-spline curves, with continuous second derivative.

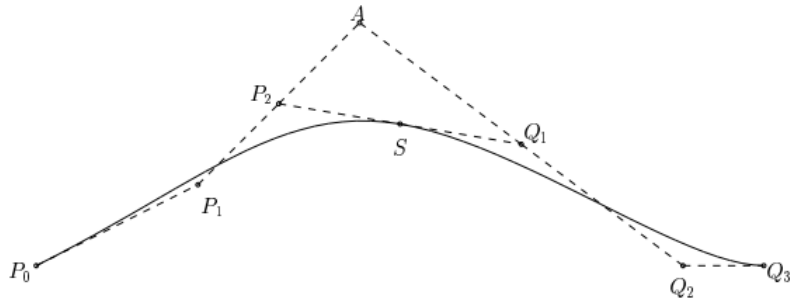


Figure 44: Example of two relaxed cubic Bézier curve glued at point S , continuous 2nd derivative.

B Curvature and curvature radius mathematical description

The curvature of a given planar curve is intuitively understood as the amount by which the curve deviates from being a straight line.

The curvature at a point of a differentiable curve is the curvature of its osculating circle, that is the circle that best approximates the curve near this point. The curvature of a straight line is zero.

The curvature is the reciprocal of radius of curvature. Therefore :

$$\kappa = \frac{1}{R} \quad (12)$$

$$\implies R = \frac{1}{\kappa} \quad (13)$$

In order to compute the curvature of the curves we use to design the waveguides of our designs, we will use the general parametrization of a curve in terms of $x(t)$ and $y(t)$.

Let us parametrize our given curve as : $\gamma(t) = \begin{pmatrix} x(t) \\ y(t) \end{pmatrix}$, in that case, the curvature becomes :

$$\kappa = \frac{x'y'' - y'x''}{(x'^2 + y'^2)^{3/2}} \quad (14)$$

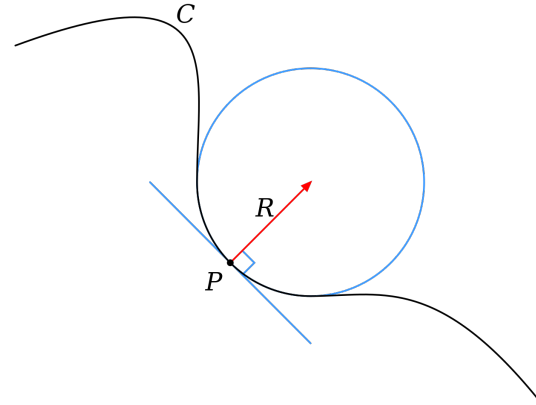


Figure 45: Example of an osculating circle of a given curve.

and by using the special case of the graph of a function, the parametrization becomes : $x = t$, $y = f(t)$, and the curvature becomes :

$$\kappa = \frac{y''}{(1 + y'^2)^{3/2}} \quad (15)$$

C Mathematical model of the buckling of the MEMS coupler

This description is based on work done by Jia-Jang Wu, from the National Kaohsiung Marine University, Taiwan [15].

The method advanced by Jia-Jang Wu that could be used to model systems in which we have a set of rigid and elastic beams, which can be implemented for finite element modeling (FEM).

The main simplification comes from the approximation that the rigid segment can be replaced by a single element for which we consider only the translational displacements in the x and y directions, and the rotation of the rigid section about the z axis (according to fig. 46). We thus are able to simplify the continuity conditions at the edges and within the beam itself, which is often the main problem when solving undecided c-c beams deflection problems.

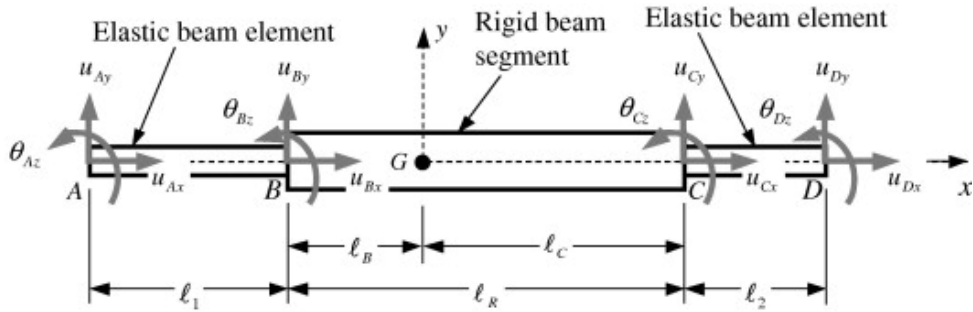


Figure 46: Approximation of the elastic-rigid-elastic beam.

It was shown that such an approximation leads to a system where the equation of motion for the system becomes :

$$[M]\{\ddot{u}\} + [K]\{u\} = \{0\} \quad (16)$$

Where $[K]$ and $[M]$ are the effective stiffness and mass matrices after imposing the clamped-clamped boundary conditions, and u is the generalized spatial coordinate. We obtain the mode shapes shown in fig. 46. The complete derivation and method is out of the scope of this research paper, but can be found in Dr. Wu's work [15].

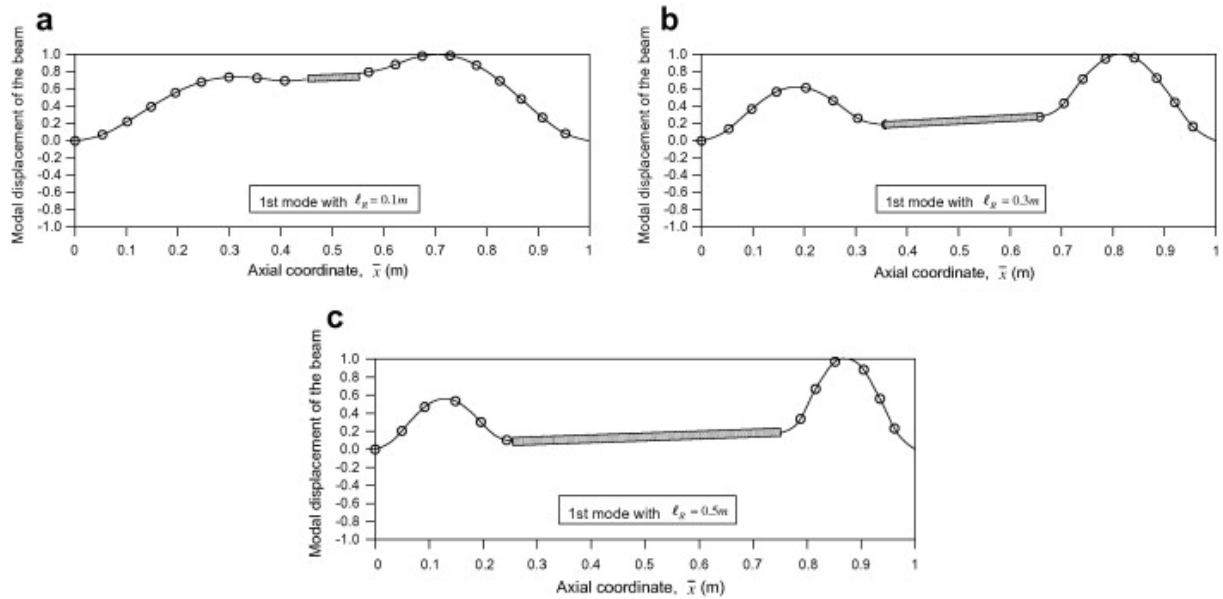


Figure 47: First mode shape for different lengths of the middle rigid section.

Using this approach it was demonstrated that for small dimensions of the rigid segment with respect to the elastic beams, and for the clamped-clamped condition, the mode shape of the beams under buckling approaches the parabolic shape expected from a fully elastic beam.